NASA-CR-152282

Flow Research Report No. 135

The Direct Numerical Simulations of the Turbulent Wakes of Axisymmetric Bodies* - An Interim Report -

By

James J. Riley

and

Ralph W. Metcalfe

Flow Research Company
A Division of Flow Industries, Inc.
21414 - 68th Avenue South
Kent, Washington 98031
(206) 854-1370

*This work was supported by NASA Ames Research Center Contract No. NAS2-9855.

Abstract

In this report, we present comparisons of results of direct numerical simulations of turbulence with both laboratory data and self-similarity theory for the case of the turbulent wakes of towed, axisymmetric bodies. In general, the agreement of the simulation results with both the laboratory data and the self-similarity theory is good, although the comparisons are hampered by inadequate procedures for initializing the numerical simulations.

Acknowledgements

The authors wish to thank several people for their help in this study; in particular, Drs. J.-T. Lin and M. Gad-el-Hak for many helpful discussions of the laboratory data, and Dr. M. W. Rubesin for guidance in selecting the proper research problem. The computer program used to perform the numerical simulations is a modification of a program originally written by Professor S. A. Orszag.

Table of Contents

1. Introduction

This paper reports the use of direct numerical simulations to study the wakes of towed, axisymmetric bodies. Most past numerical work on turbulence has employed the Reynolds-averaged equations of motion, which are necessarily supplemented by a series of ad hoc assumptions. However, direct numerical simulations of turbulence involve the numerical solution of the fundamental equations of motion to obtain the detailed structure of the turbulent field. What is obtained from the calculations, then, is the time history of the very complex turbulent velocity field. This method is analogous to performing experiments in the laboratory, and statistical results can be obtained by temporal, spatial, and/or ensemble averaging over the computed flow field.

Some of the earliest work using direct numerical simulations of turbulence was applied to low enough Reynolds numbers ($R_\lambda \lesssim 50$, see, e.g., Orszag and Patterson, 1972) so that all the dynamically significant scales of motion were adequately resolved by the numerical algorithm. For higher Reynolds number flows, however, there is no hope to resolve all the relevant scales of motion using computers available either now or in the near future. Thus, for high Reynolds number flows, the meteorologists' approach to numerical weather prediction is followed. In this approach, the smaller, subgrid-scale motions, which cannot be resolved on the computational mesh, are filtered out of the fundamental equations. Only the grid-scale motions are computed directly. (For this reason, when direct numerical simulations are applied to higher Reynolds number flows, the technique is sometimes referred to as large eddy simulations.) This filtering process introduces subgrid-scale effects in the form of stresses which are analogous to Reynolds stress terms appearing in the Reynolds-averaged equations of motion.

The subgrid-scale stresses are normally modeled in a manner analagous to the modeling of the Reynolds stresses. There is reason to believe, however, that the subgrid-scale modeling will have a better chance of success than conventional turbulence modeling. First, the smaller scale turbulent motions behave in a more universal manner than

the larger scale motions. Hence, it is more likely that a single model for the subgrid-scale stresses may be applicable to a broad class of flows. Second, the subgrid-scale motions usually contain only a small portion of the turbulence energy, so that the modeled terms have less influence on the overall dynamics than the Reynolds stresses. Thus, this approach may overcome some of the drawbacks to the conventional approach to computing turbulent flows using the Reynolds-averaged equations. This technique, however, will always possess the disadvantage that a more difficult numerical problem must be treated, which is necessarily three-dimensional and time-dependent, and for which greater spatial and temporal resolution is necessary.

As mentioned, this procedure is analogous to performing experiments in the laboratory. However, it has the advantages that (i) much more statistical information of interest can be obtained (since the entire flow field is known at every time step), (ii) parameters can be varied easily, and (iii) experimental conditions are more controllable. The technique also offers the advantage of circumventing the closure problems that have plagued turbulence theory. Because of these advantages, direct numerical simulations of turbulence can serve a variety of purposes. For example, they can be usefully employed to test theories from the more exotic (e.g., the direct interaction approximation) to Reynolds stress closure models. They can also be very useful in obtaining a better understanding of the underlying physical processes. And these simulations may be ultimately used as a predictive technique for applied problems. However, before this approach can be used with confidence, especially when applied to high Reynolds number flows, its validity and accuracy under various conditions need to be determined through careful comparison of the results of the simulations with experimental data.

Some work has been carried out with the purpose of establishing the validity and accuracy of numerical simulations of turbulence. For example, research at Stanford and NASA Ames (Mansour et al., 1977; Ferziger et al., 1977) has led to the successful prediction of the large-scale features of homogeneous turbulence decay. There has also been some success in the comparison of simulation results with channel flow data (Deardorff, 1970; Grotzbach and Schumann, 1977). However, in

these studies the flow in the region near the wall, where many of the physical processes of current interest occur, was modeled. Recent work by Moin et al. (1978) has examined removing this latter limitation by computing the flow in the entire boundary layer. While significant contributions have been made in establishing the validity and accuracy of numerical simulations, it is apparent that much more work needs to be done to establish the capabilities of the method.

The study of free shear flows may offer an excellent vehicle for determining the capabilities of direct numerical simulations to treat turbulent shear flows. While possessing many of the dynamic processes of all turbulent flows, free shear flows are generally easier to treat numerically than bounded flows. This is because, first of all, the boundary conditions are usually easier to implement numerically, and secondly, the resolution requirements are much less stringent. In particular, the powerful pseudospectral numerical methods can be easily applied to some free shear flows.

We have chosen to study the wakes of axisymmetric, slender, towed bodies. This choice was made for several reasons. First, there is extensive data available for this case (e.g., Chevray, 1968; Pao and Lin, 1973; Bukreev et al., 1972). Secondly, as long as (i) the mean velocity deficit is small with respect to the body speed, and (ii) the lateral scale of nonhomogeneity is small with respect to the axial length scale, then it can be shown (see Section 2.3) that this flow can be treated as a time-dependent problem (with time interpreted as axial variation in the data) which is statistically homogeneous in the axial direction. This leads to significant simplifications in the numerical procedures, and also gives us the opportunity to study a statistically time-dependent flow. The two conditions described above are satisfied in the late wake in the experiments. Another advantage of late wakes of axisymmetric bodies is that they appear to be approximately self-preserving, so that the flow develops in a fairly simple manner. For example, Figure 1 is a plot from Pao and Lin (1973) showing the collapse of

several sets of data in the late wake, and also the agreement of the data with the self-preserving decay rate*.

The main objective of the work presented is the determination of how well direct numerical simulations can model a simple turbulent shear flow. Our method of approach is to initialize our calculations with available wake data at a specific location downstream of the body, and then compute the subsequent development of the wake. The results of the numerical simulations are then compared with data downstream of the original plane to determine how well the wake has been simulated. The effects of a subgrid-scale model (or lack of one), of the initialization procedure, of the numerical algorithms and other features of the simulations are examined.

In the next section we discuss the techniques that we used (e.g., numerical methods and initialization procedures) to simulate axisymmetric wakes. In Section 3 we present the results of our simulations and comparisons with laboratory data. Section 4 contains a discussion of alternative initialization procedures. Finally, in Section 5 we present our conclusions and recommendations.

*In this plot, U_m is the maximum axial mean velocity, U_o the body speed, x is axial distance measured from the body stern, D is maximum body diameter, C_D is the drag coefficient, and $R_D = \frac{U_o D}{\nu}$, where ν is the kinematic viscosity.

2. Method of Approach

Before examining the results of our simulations, it is important to first understand the methods used to perform the simulations. These methods involve specifically the numerical techniques, the subgrid-scale model, the $x \to t$ transformation used to relate the simulations to laboratory data, and the initialization procedures. These topics will be addressed in this section.

2.1 Numerical Methods

The numerical methods used to solve the Navier-Stokes equations are the same as employed by Orszag and Pao (1974). The Navier-Stokes equations are written in rotational form:

$$\frac{\partial}{\partial t}\underset{\sim}{u} - \underset{\sim}{u} \times \underset{\sim}{\omega} = -\frac{1}{\rho}\nabla p_D + \nu \nabla^2 \underset{\sim}{u} \tag{1}$$

$$\nabla \cdot \underset{\sim}{u} = 0 \tag{2}$$

where $\underset{\sim}{\omega} = \nabla \times \underset{\sim}{u}$ is the vorticity vector, and (3)

$$p_D = p + \frac{1}{2}\rho |\underset{\sim}{u}|^2 \tag{4}$$

is the dynamic pressure. This form of the equation ensures energy conservation in our numerical scheme.

The initial conditions will be discussed in detail in Section 2.4. The wake is chosen to be situated so that the axial direction, the direction of non-zero mean flow, is taken to be the x_1 direction (Figure 2). As discussed below, the flow will be assumed to be statistically homogeneous in this direction. Periodic boundary conditions have

been successfully employed in the past along directions of statistical homogeneity (see, e.g., Orszag and Patterson, 1972), so we choose periodic boundary conditions in this direction. In the radial (x_2 and x_3) direction, there is no mean flow (see Section 2.3) so that inflow-outflow conditions are not necessary there. Thus, for convenience, and also to employ pseudospectral numerical methods most easily, periodic boundary conditions are also used in the lateral direction (x_2) and periodic no-stress (free-slip) conditions in the vertical (x_3). The latter conditions are used because the computer program also was written to treat density stratification effects in the vertical direction.

Pseudospectral methods are used to solve the governing equations*. The equations are solved on a 32 x 32 x 33 grid in physical space. The pseudo-spectral method involves the evaluation of the derivatives using the Fourier expansions, i.e., if

$$u(x) = \sum_{|k|<K} \hat{u}(k)\, e^{ikx}, \tag{5}$$

then $\frac{\partial u}{\partial x}$ is evaluated as

$$\frac{\partial u}{\partial x} = \sum_{|k|<K} ik\, \hat{u}(k)\, e^{ikx}. \tag{6}$$

The method is similar to the spectral method except that aliasing effects which arise in the computation of the nonlinear terms are not excluded (e.g., Fox and Orszag, 1973). The method appears to be as accurate as the spectral method, however, and is roughly a factor of 2 more efficient computationally.

The computations presented herein were performed on the NASA Ames CDC 7600. The calculations require about 3 sec/time step for the 32 x 32 x 33 computational mesh. The numerical algorithm uses fast Fourier

*Pseudospectral methods are approximately twice as accurate in each space dimension as comparable finite different schemes with the same resolution, and are competitive in computational efficiency for problems with simple geometry. Thus, they offer significant advantages when applied to problems of the type described here (Orszag and Israeli, 1974).

transform methods to evaluate transforms and inverse transforms, and uses leapfrog time differencing on the nonlinear terms, and Crank-Nicolson (implicit) time differencing on the viscous terms.

The numerical simulation data presented is mostly in the form of spatial averages. To perform these averages, we take advantage of the axial homogeneity and axisymmetry and divide the flow field into concentric annuli with axes along the x_1 axis (Figure 3). The gap width of each annulus is taken to be the mesh spacing (Δx_1). The average value of a quantity q in the n^{th} annulus is obtained by summing the values of q for each grid point in the annulus, and then dividing by the total number of points in the annulus, e.g.,

$$\text{Average}(q) = \frac{1}{N_n} \sum_{i=1}^{N_n} q_i \ , \tag{7}$$

where N_n is the number of grid points in the n^{th} annulus. In Table 1, we show N_n for each n, and also $\frac{1}{\sqrt{N_n}}$, which is roughly proportional to the statistical error expected in computing an average. Note that the error is expected to decrease substantially with increasing distance from the x_1 axis, until the annuli intersect the boundaries of the computational domain.

2.2 Subgrid-Scale Modeling

The basic idea of direct numerical simulations of turbulence is to numerically compute the detailed evolution of the complex turbulent velocity field. Because the simulations are inherently three-dimensional, the best possible numerical resolution using present-day computers would span about one to two decades in wave number space. However, the laboratory data that we choose to model (Pao and Lin, 1973) has significant interactions occurring over many decades. It is obvious that the simulations cannot treat all the details of this flow.

In order to handle the smaller scale motions which cannot be resolved in the computer simulations, subgrid-scale modeling is usually introduced. This method was first suggested by Smagorinsky et al. (1965)

for general circulation models of the atmosphere, while Lilly (1967) first studied its use in turbulence simulation. To employ subgrid-scale modeling, the Navier Stokes equations, (1) and (2), are first filtered to eliminate the smaller scale motions. Generally a spatial average is used, of the form

$$\langle \underset{\sim}{u}(\underset{\sim}{x},t)\rangle = \int_R G(\underset{\sim}{x}-\underset{\sim}{x}')\,\underset{\sim}{u}(\underset{\sim}{x}',t)\,d\underset{\sim}{x}', \tag{8}$$

where G is a filter function and R encompasses the entire flow domain (see, e.g., Leonard, 1974). Here we have used the symbol $\langle \underset{\sim}{u}\rangle$ to denote the filtered value of the vector $\underset{\sim}{u}$. The flow variables can thus be expressed as a filtered part, or large scale part, $\langle \underset{\sim}{u}\rangle$, and a subgrid-scale component, say $\underset{\sim}{u}'$. Thus

$$\underset{\sim}{u} = \langle \underset{\sim}{u}\rangle + \underset{\sim}{u}' . \tag{9}$$

When (9) is substituted into equations (1) and (2), and the filtering operation is performed on the equations, there results

$$\frac{\partial}{\partial t}\langle u_i\rangle + \frac{\partial}{\partial x_j}\langle\langle u_i\rangle\langle u_j\rangle\rangle = -\frac{1}{\rho}\frac{\partial}{\partial x_i}\langle p\rangle + \nu\nabla^2\langle u_i\rangle - \frac{\partial}{\partial x_j}\left[\langle u_i' u_j'\rangle + \langle\langle u_i\rangle u_j'\rangle + \langle u_i'\langle u_j\rangle\rangle\right] \tag{10}$$

$$\frac{\partial}{\partial x_i}\langle u_i\rangle = 0 \tag{11}$$

Note that, in general, $\langle\langle \underset{\sim}{u}\rangle\rangle \neq \langle \underset{\sim}{u}\rangle$.

Equations (10) and (11) are the dynamic equations for the resolvable (large eddy) motions. The last term in equation (10) represents the effect of the filtered (subgrid-scale) motions on the large scale motions. Clearly a closure problem, analogous to that resulting from Reynolds averaging of the original equations, has resulted from the filtering process.

In order to proceed further, the effect of the subgrid-scale motion on the resolvable scales needs to be modeled. Smagorinsky et al. (1965), realizing the analogy with the Reynolds averaging, modeled the subgrid-scale stresses using the eddy viscosity concept. Deardorff (1974a, 1974b) generalized this by introducing equations for higher order subgrid-scale quantities, e.g., for the subgrid-scale kinetic energy and subgrid-scale stresses. Leonard (1974) put this work on a firm theoretical foundation by carefully defining the averaging procedures and separating out the different effects. In more recent years, there has been considerable activity in this problem area, from finding theoretical justification for the models (e.g., Love and Leslie, 1977) to careful comparisons with data (e.g., McMillan and Ferziger, 1978).

Orszag (1974) has suggested an alternative to the subgrid-scale procedure which might be applicable to free shear flows. It is based on the concept of Reynolds number similarity, which is that if the Reynolds number of a free shear flow is high enough, then the statistical properties which depend on the large-scale features of that flow (e.g., turbulent energy, Reynolds stress) will be independent of Reynolds number. As the Reynolds number of a free shear flow is increased, the wave number range over which viscous dissipation occurs becomes widely separated from the wave numbers containing the bulk of the turbulent energy. (Figure 4.) For example, the ratio of the dissipation scale,

$$K_D = (\varepsilon/\nu^3)^{1/4} \approx \left(\frac{u'^3}{\ell\nu^3}\right)^{1/4},$$

to the energy containing scale, $K_e = \ell^{-1}$, is

$$\frac{K_D}{K_e} \approx \left(\frac{u'^3}{\ell\nu^3}\right)^{1/4} \ell = \left(\frac{u'\ell}{\nu}\right)^{3/4} \equiv R_\ell^{3/4}. \qquad (12)$$

(Here u' is a characteristic turbulence velocity and ℓ is a characteristic length scale of the energetic turbulence.) Generally, R_ℓ is several orders of magnitude or more so that the energy and dissipation scales are widely separate. It is argued that the nonlinear interactions are somewhat local in wave number space, so that the large

eddies are not directly affected by the dissipation scale motions. Thus the larger scale motions are essentially inviscid, and transfer their energy to smaller scales, to be ultimately dissipated by the much smaller scale motion. Thus the large scale behavior of these flows should be inviscid, independent of the Reynolds number. Hence, the term Reynolds number similarity.

Reynolds number similarity has been experimentally established for the decay of grid turbulence (see, e.g., Townsend, 1976). Also, recent experiments on turbulent shear layers has lent support for this principle (see Roshko, 1976, for a review of this work). Visualization studies have shown the qualitative similarity of the large-scale structure of these flows for a broad range of Reynolds numbers. Quantitative data from these experiments also supports the principle. Furthermore, the application self-similarity theory to turbulent wakes, which implicitly includes the Reynolds-number-independence hypothesis, gives results which agree well with laboratory data. This last point will be discussed in more detail in section 2.3.

Past numerical simulations of turbulence which have not used subgrid-scale modeling, but which have resolved all the dynamically significant scales, have been successful for values of R_λ up to about 50, where R_λ is the Reynolds number based upon the Taylor microscale λ. (This is still a fairly low-to-moderate value for laboratory studies. For example, Chevray's (1968) Reynolds number was about 700, Pao and Lin's (1973) was about 90, and Champagne, et al. (1979) reported a value of 130 in their homogeneous shear flow experiments.) It is possible that this Reynolds number is high enough for the flow to be approximately Reynolds number independent. We concluded that this was an important possibility to address. Thus, in the work presented in this report, no subgrid-scale model was used. The R_λ was initialized to be roughly 50, and we hoped to conclude whether this was large enough for Reynolds number similarity to hold. We plan in the future to recompute these cases using a subgrid-scale model, in order to determine the difference in the two approaches. Finally, one might consider our approach, i.e., assuming Reynolds number similarity and computing a flow with much lower Reynolds number, but with all the scales resolvable, as a very simple subgrid-scale model.

2.3 Self-Similarity

In order to examine axisymmetric wakes further, it is useful to use cylindrical polar coordinates. We use the (r,θ,x) coordinate system shown in Figure 2, where r is the radial coordinate, θ is the circumferential coordinate, and x the axial coordinate (measured from the body stern), taken to be positive in the direction opposite that of the body motion. Let $(u_r\ ,\ u_\theta\ ,\ u_x)$ denote the corresponding velocities. Then equations (1) and (2) are

$$\frac{\partial}{\partial t}u_r + u_r\frac{\partial}{\partial r}u_r + \frac{u_\theta}{r}\frac{\partial}{\partial\theta}u_r - \frac{u_\theta^2}{r} + u_x\frac{\partial}{\partial x}u_r = -\frac{1}{\rho}\frac{\partial}{\partial r}p \qquad (13)$$
$$+\nu\left[\frac{\partial}{\partial r}\left(\frac{1}{r}\frac{\partial}{\partial r}(ru_r)\right) + \frac{1}{r^2}\frac{\partial^2}{\partial\theta^2}u_r - \frac{2}{r^2}\frac{\partial}{\partial\theta}u_\theta + \frac{\partial^2}{\partial x^2}u_r\right]$$

$$\frac{\partial}{\partial t}u_\theta + u_r\frac{\partial}{\partial r}u_\theta + \frac{u_\theta}{r}\frac{\partial}{\partial\theta}u_\theta + \frac{u_r u_\theta}{r} + u_x\frac{\partial}{\partial x}u_\theta = -\frac{1}{\rho r}\frac{\partial}{\partial\theta}p \qquad (14)$$
$$+\nu\left[\frac{\partial}{\partial r}\left(\frac{1}{r}\frac{\partial}{\partial r}(ru_\theta)\right) + \frac{1}{r^2}\frac{\partial^2}{\partial\theta^2}u_\theta + \frac{2}{r}\frac{\partial}{\partial\theta}u_r + \frac{\partial^2}{\partial x^2}u_\theta\right]$$

$$\frac{\partial}{\partial t}u_x + u_r\frac{\partial}{\partial r}u_x + \frac{u_\theta}{r}\frac{\partial}{\partial\theta}u_x + u_x\frac{\partial}{\partial x}u_x = -\frac{1}{\rho}\frac{\partial}{\partial x}p \qquad (15)$$
$$+\nu\left[\frac{1}{r}\frac{\partial}{\partial r}\left(r\frac{\partial}{\partial r}u_x\right) + \frac{1}{r^2}\frac{\partial^2}{\partial\theta^2}u_x + \frac{\partial^2}{\partial x^2}u_x\right]$$

$$\frac{1}{r}\frac{\partial}{\partial r}(ru_r) + \frac{1}{r}\frac{\partial}{\partial\theta}u_\theta + \frac{\partial}{\partial x}u_x = 0. \qquad (16)$$

In order to obtain the Reynolds-averaged equation of motion, we decompose the velocity vector and pressure into (ensemble) mean and fluctuating parts, i.e.,

$$(u_r, u_\theta, u_x) = (W+w, V+v, U+u) \qquad (17)$$

$$p = P + p. \qquad (18)$$

Substituting (17) and (18) into (13) to (16), ensemble averaging, and assuming statistical stationarity and axisymmetry, and no swirl (V=0) gives*

$$W\frac{\partial}{\partial r}W + U\frac{\partial}{\partial x}W = -\frac{1}{\rho}\frac{\partial}{\partial r}P + \nu\left[\frac{\partial}{\partial r}\left(\frac{1}{r}\frac{\partial}{\partial r}(rW)\right) + \frac{\partial^2}{\partial x^2}W\right] - \frac{1}{r}\frac{\partial}{\partial r}(r\overline{w^2}) - \frac{\partial}{\partial x}(\overline{uw}) \tag{19}$$

$$W\frac{\partial}{\partial r}U + U\frac{\partial}{\partial x}U = -\frac{1}{\rho}\frac{\partial}{\partial x}P + \nu\left[\frac{1}{r}\frac{\partial}{\partial r}\left(r\frac{\partial U}{\partial r}\right) + \frac{\partial^2}{\partial x^2}U\right] - \frac{1}{r}\frac{\partial}{\partial r}(r\overline{uw}) - \frac{\partial}{\partial x}(\overline{u^2}) \tag{20}$$

$$\frac{1}{r}\frac{\partial}{\partial r}(rW) + \frac{\partial}{\partial x}U = 0 \tag{21}$$

Equations for the higher order quantities (e.g., $\overline{u^2}$, $\overline{uw}$, $\overline{w^2}$) can be obtained by subtracting equations (19) and (20) from (13) and (15) to obtain equations for the fluctuating components, multiplying by w, v, or u, and ensemble averaging (see, e.g., Tennekes and Lumley, 1972). Statistical stationarity implies that we have fixed our coordinate system to be moving with the body, at a speed relative to the fluid which we call U_o.

We are interested mainly in the far wake of an axisymmetric body where the flow is approximately self-similar. In this region the following conditions are approximately satisfied (see Tennekes and Lumley, 1972, for a more detailed discussion of self-similarity):

i. The axial variation of any statistical quantity $(\overline{q})$ is much smaller than its radial variation, i.e.,

$$\frac{\partial}{\partial x}\overline{q} \ll \frac{\partial}{\partial r}\overline{q}\ , \text{ or}$$

*An overbar (¯) will be used throughout this text to denote an ensemble average.

$$\ell_x >> \ell_r \ ,$$

where ℓ_x and ℓ_r are characteristic length scales of axial and radial variations in mean quantities;

ii. The maximum value over which the mean velocity varies, say U_m, is much smaller than the body speed,

$$U_m << U_o \ ;$$

iii. The Reynolds number of the flow, $\frac{U_m \ell_r}{\nu}$, is large enough so that the viscous diffusion terms in equations (19) and (20) can be neglected with respect to turbulence diffusion terms.

With these conditions, equation (20) reduces to approximately*

$$U_o \frac{\partial}{\partial x} U + \frac{1}{r} \frac{\partial}{\partial r} (r \overline{uw}) = 0. \tag{22}$$

Following the self-similarity theory, we assume the axial mean velocity and the Reynolds stress to be of the form**

$$U(r,x) = U_m(x) u(\eta) \tag{23}$$

$$\overline{uw}(r,x) = U_m^2(x) s(\eta) \ , \tag{24}$$

---

*Scaling equation (21) results in $\frac{W}{U} \sim \frac{\ell_r}{\ell_x}$, so that W is small with respect to U in the late wake.

**In everything that follows, we take U to be the axial mean velocity deficit, i.e., the difference between the axial mean velocity, measured in a coordinate system moving with the body, and the free stream velocity U_o.

where $\eta = \frac{r}{\zeta(x)}$ is the similarity variable. The velocity scale U_m and the length scale ζ are to be determined. When (23) and (24) are used in (22), and the further condition derived from (22),

$$\frac{\partial}{\partial x}\int_0^\infty r U\, dr = \text{constant} \tag{25}$$

is imposed, there results

$$U_m(x) = A x^{-2/3} \tag{26}$$

$$\zeta(x) = B x^{1/3}, \tag{27}$$

where A and B are constants to be determined empirically. Therefore, for the flow in the wake to remain self-similar, the velocity scale (e.g., peak velocity) should decay as $x^{-2/3}$, and the length scale should increase as $x^{1/3}$.

To go any further, a closure assumption is needed. Following mixing-length theory we let

$$\overline{uw} = -\nu_T \frac{\partial}{\partial r} U, \text{ where} \tag{28}$$

$$\nu_T = C \zeta U_m, \tag{29}$$

and C is a constant to be determined empirically.* Then equation (22) can be solved to give

$$u(\eta) = \exp\left(-\frac{B}{4AC}\eta^2\right) \tag{30}$$

$$s(\eta) = \frac{B}{2A}\eta \exp\left(-\frac{B}{4AC}\eta^2\right) \tag{31}$$

*Note that this closure assumption does not include dependence of $\overline{uw}$ on viscosity, i.e., Reynolds number similarity has been implicitly assumed.

Equations (26), (27), (30) and (31) are the main results from the self-similarity theory.

Defining the total crossplane mean kinetic energy E by

$$E = \int_0^{2\pi} r\,d\theta \int_a^{\infty} dr\, \rho \frac{U^2}{2}, \tag{32}$$

and the total crossplane turbulent energy e by

$$e = \int_0^{2\pi} r\,d\theta \int_a^{\infty} dr\, \frac{\rho}{2}\left(\overline{u^2} + \overline{v^2} + \overline{w^2}\right), \tag{33}$$

then self-similarity theory can also be used to determine the axial behavior of E and e. Substituting (26) and (27) into (23), and (23) into (32), and integrating gives

$$E(x) = D x^{-2/3}, \tag{34}$$

where D is an empirical constant. Following a similar procedure for e yields

$$e(x) = F x^{-2/3}, \tag{35}$$

where F is another empirical constant.

The approximate validity of the self-similarity theory can be established by comparing conclusions from the theory with experimental data. Figure 5 is a plot from Pao and Lin (1973) showing the growth of the mean velocity wake radius (r_m) for several different sets of data for the wakes of axisymmetric bodies.* There is fairly good agreement with the theory for each set of data. Figure 1 is a plot of the decay of the maximum mean velocity (U_m) for the same data sets (again extracted from Pao and Lin). Again the agreement with the theory is good. Figure 6 gives the radial behavior of the axial mean velocity in Pao and Lin's data. The solid line is the self-similarity prediction, equation (30), using an eddy viscosity assumption. The agreement of theory and experiment

*The mean wake radius r_m is defined here as the distance from the mean velocity peak (at $r = 0$) to the point at which the mean velocity attains half its peak value.

here is also good. Similar results have also been demonstrated (e.g., Pao and Lin) for the behavior of the axial component of the turbulence intensity $\overline{u^2}$, the radial component $\overline{w^2}$, and the Reynolds stress $\overline{uw}$. It is apparent that self-similarity theory is approximately valid in the far wakes in these experiments.

The existence of a self-similar far wake region, and the implied conditions necessary, provide the basis for the present calculations. In the far wake, assuming conditions (i) and (ii) are satisfied, the statistical equations can be obtained from the original equations by neglecting all derivatives with respect to x, except when multiplied by U_o. Thus the axial mean momentum equation (20) reduces to

$$U_o \frac{\partial}{\partial x} U = \nu \frac{1}{r} \frac{\partial}{\partial r}\left(r \frac{\partial}{\partial r} U\right) - \frac{1}{r} \frac{\partial}{\partial r}\left(r \overline{uw}\right). \tag{36}$$

The Reynolds averaged equation for the axial component of the turbulence intensity is

$$\begin{aligned} W \frac{\partial}{\partial r}\left(\frac{\overline{u^2}}{2}\right) + \left(U_o + U\right) \frac{\partial}{\partial x}\left(\frac{\overline{u^2}}{2}\right) + \overline{uw} \frac{\partial}{\partial r} U + \overline{u^2} \frac{\partial}{\partial x} U + \frac{1}{r} \frac{\partial}{\partial r}\left(r \frac{\overline{u^2 w}}{2}\right) \\ + \frac{\partial}{\partial x}\left(\frac{\overline{u u^2}}{2}\right) = -\frac{1}{\rho} \overline{u \frac{\partial}{\partial x} p} + \nu\left[\frac{1}{r} \frac{\partial}{\partial r}\left(r \frac{\partial}{\partial r}\left(\frac{\overline{u^2}}{2}\right)\right) + \frac{\partial^2}{\partial x^2}\left(\frac{\overline{u^2}}{2}\right)\right] \\ - \nu\left[\overline{\left(\frac{\partial u}{\partial r}\right)^2} + \frac{1}{r^2} \overline{\left(\frac{\partial u}{\partial \theta}\right)^2} + \overline{\left(\frac{\partial u}{\partial x}\right)^2}\right]. \end{aligned} \tag{37}$$

With the far-field scaling, this reduces to

$$\begin{aligned} U_o \frac{\partial}{\partial x}\left(\frac{\overline{u^2}}{2}\right) + \overline{uw} \frac{\partial}{\partial r} U + \frac{1}{r} \frac{\partial}{\partial r}\left(r \frac{\overline{u^2 w}}{2}\right) = -\frac{1}{\rho} \overline{u \frac{\partial}{\partial x} p} \\ + \nu \frac{1}{r} \frac{\partial}{\partial r}\left(r \frac{\partial}{\partial r}\left(\frac{\overline{u^2}}{2}\right)\right) - \nu\left[\overline{\left(\frac{\partial u}{\partial r}\right)^2} + \frac{1}{r^2} \overline{\left(\frac{\partial u}{\partial \theta}\right)^2} + \overline{\left(\frac{\partial u}{\partial x}\right)^2}\right]. \end{aligned} \tag{38}$$

Similar equations can be obtained for the other turbulence quantities.

If $\frac{x}{U_o}$ is interpreted as time, it is easy to see that (36) and (38) are <u>identical</u> to the corresponding equations for a time dependent, axisymmetric flow without mean swirl, which is statistically homogeneous in the axial (x) direction. This can be shown to be true for all other statistical equations, and is a result of the fact that, in the far-field approximation, x derivatives are only retained when multiplied by U_o.

It is much easier to numerically treat a problem which is statistically homogeneous in the axial direction and time-dependent, than to compute a flow which is statistically steady, but nonhomogeneous in the axial direction. In the latter case we have to deal with complex upstream inflow and downstream outflow boundary conditions. Also in the far field, the mean radial velocity is negligible with respect to the mean axial velocity, so that we need not be concerned with radial inflow boundary conditions. Thus, in the present simulations, we choose to compute the statistically axially homogeneous, time-dependent problem. Time, in our calculations, is interpretable as $\frac{x}{U_o}$ in the laboratory data.

Note that if the far-field assumptions break down, i.e., if U_m is not small with respect to U_o, or if the radial scale (ℓ_r) is not small with respect to the longitudinal scale (ℓ_x), then it is not proper to replace the steady-state wake with a horizontally homogeneous, time-dependent wake. This is particularly true in the near field where

$$U_m \sim U_o, \text{ and}$$
$$\ell_r \sim \ell_x .$$

Another way to see the justification for considering the time-dependent problem is the following. Fix the coordinate system with fluid. Shortly after the body goes by, the mean convection terms (e.g., $W \frac{\partial}{\partial r}(\ )$, $U \frac{\partial}{\partial x}(\ )$) are important. Later on, however, as the mean velocity decays, they become negligible. It is then possible to compute the time history of a slab of fluid, and, when comparing with data, treat time as $\frac{x}{U_o}$. Because $\frac{\ell_r}{\ell_z}$ is small in the late wake, axial derivatives of mean quantities can be neglected.

2.4 Initialization Procedure

To initialize the velocity field, we use the data of Pao and Lin (1973) at $x/D = 36$. This downstream location is in the early stages of the approximately self-preserving region. We first separate the

velocity field $\underset{\sim}{u}$ into a mean component and a turbulence component as given by equation (17), i.e.,

$$(u_r, u_\theta, u_x) = (W + w, V + v, U + u). \tag{17}$$

In the self-preserving regime, the only nonzero component of the mean velocity is the axial component, U. An excellent approximation to the axial mean velocity profile in the data is given by the self-similar formula (figure 6),

$$U(r,x) = U_m(x) \exp\left[-.693 \frac{r^2}{r_m^2(x)}\right], \tag{39}$$

where U_m is the maximum value of U, and r_m is defined by

$$U(r_m(x), x) = \frac{1}{2} U_m(x). \tag{40}$$

We use

$$(W, V, U) = \left(0, 0, \mathcal{U} \exp\left(-.693 \frac{r^2}{\mathcal{R}^2}\right)\right), \tag{41}$$

$$\text{where } \mathcal{U} = U_m\big|_{x/D = 36}, \tag{42}$$

$$\mathcal{R} = r_m\big|_{x/D} = 36. \tag{43}$$

as initial conditions for our mean velocity field.

To initialize the turbulent velocity field, we use the method suggested by Orszag and Pao (1974). It is an adaptation to nonhomogeneous turbulent flows of the method of Orszag and Patterson (1972), which is applicable to homogeneous turbulent flows. We will briefly explain the latter first, and then show how the former method is a modification of it.

In order to ensure incompressibility, Orszag and Patterson write the velocity field as the curl of a stream function vector $\underset{\sim}{\psi}$,

$$\underset{\sim}{u} = \nabla \times \underset{\sim}{\psi}. \tag{44}$$

(Note that this greatly restricts the class of velocity fields considered, since in general an arbitrary velocity field can be expressed as the sum of an irrotational part $(\nabla\phi)$ and a rotational part $(\nabla\times\underset{\sim}{\psi})$; see, e.g., Batchelor, 1967.) The velocity field is expanded in a discrete Fourier series,

$$\underset{\sim}{u}(\underset{\sim}{x}) = \sum_{|\underset{\sim}{k}|<K} \hat{\underset{\sim}{u}}(\underset{\sim}{k})\, e^{i\underset{\sim}{k}\cdot\underset{\sim}{x}} \tag{45}$$

and (44) becomes

$$\hat{\underset{\sim}{u}}(\underset{\sim}{k}) = i\,\underset{\sim}{k}\times\hat{\underset{\sim}{\psi}}\,, \tag{46}$$

where $\hat{\underset{\sim}{\psi}}$ is the discrete Fourier transform of $\underset{\sim}{\psi}$. The energy spectrum for $\hat{\underset{\sim}{\psi}}$ is determined uniquely by the energy spectrum for $\underset{\sim}{u}$. The Fourier amplitudes $\hat{\underset{\sim}{\psi}}$ for each $\underset{\sim}{k}$ are chosen to be Gaussianly distributed with zero mean, and the standard deviation chosen to produce the proper spectrum for $\underset{\sim}{\psi}$, and hence for $\underset{\sim}{u}$. To ensure homogeneity, the Fourier amplitudes for differing wave numbers are chosen to be statistically independent. For statistically isotropic flows, the components of a particular Fourier mode are taken to be statistically independent but identically distributed. Note that, because the initial velocity field is comprised of a large sum of statistically independent terms, from the Central Limit Theorem (e.g., Feller, 1957) we know that it has a joint normal probability distribution.

The velocity field for a particular realization is set up by first numerically selecting each Fourier amplitude $\hat{\underset{\sim}{\psi}}$ from its proper ensemble using a pseudo-random number generator. Then $i\underset{\sim}{k}\times\hat{\underset{\sim}{\psi}}$ is formed to give $\hat{\underset{\sim}{u}}$, and finally the inverse discrete transform is performed to give $\underset{\sim}{u}$.

The modification of Orszag and Pao (1974) also starts by first generating the Fourier amplitude $\hat{\underset{\sim}{\psi}}$. However, $\hat{\underset{\sim}{\psi}}$ is then transformed to physical space to produce $\underset{\sim}{\psi}$, multiplied by a form function, $J(r)$ for the case of an axisymmetric wake, and the product is transformed back to Fourier space. The cross product with $i\underset{\sim}{k}$ is then taken to

ensure incompressibility. The velocity field obtained from this series of operations is then

$$\underset{\sim}{u} = \nabla \times \left(J \underset{\sim}{\psi} \right) . \tag{47}$$

We choose the stream function field $\underset{\sim}{\psi}$ to be statistically isotropic. Then its energy spectrum can be expressed as

$$E_\psi (k) = \frac{3}{2k^2} E_u(k) , \tag{48}$$

where $E_u(k)$ is the energy spectrum for a statistically homogeneous, isotropic field obtained by the method of Orszag and Patterson. The resulting velocity field defined by equation (47) has the following moments:

$$\overline{u} = \overline{v} = \overline{w} = 0 \tag{49}$$

$$\overline{u^2} = \overline{v^2} = u_0^2 \left(J^2 + \frac{\psi}{2u_0^2} \left(\frac{dJ}{dr} \right)^2 \right) \tag{50}$$

$$\overline{w^2} = u_0^2 J^2 \tag{51}$$

$$\overline{uv} = \overline{uw} = \overline{vw} = 0 , \text{ where} \tag{52}$$

$$\frac{3}{2} u_0^2 = \int_0^\infty E_u(k)\, dk , \quad \frac{3}{2} \psi_0^2 = \int_0^\infty E_\psi (k)\, dk . \tag{53}$$

Furthermore, although it is difficult to obtain a general expression for the one-dimensional axial energy spectrum, this spectrum at $r = 0$ can be shown to be identical to the one-dimensional spectrum obtained from $E_u(k)$ for the homogeneous, isotropic case.

In order to initialize the turbulent velocity, we need to select the proper energy spectrum E_u and form function $J(r)$. We choose the energy spectrum $E_u(k)$ to be given by

$$E_u(k) = \frac{8}{\pi} u_0^2 \Lambda \frac{k^4 \Lambda^4}{(1+k^2\Lambda^2)^3} . \tag{54}$$

Along $r = 0$, this produces a one-dimensional axial spectrum for the axial velocity u

$$E_{11}(k_1) = \frac{1}{\pi} u_o^2 \Lambda \frac{1 + 3k_1^2\Lambda^2}{(1 + k_1^2\Lambda^2)^2} \quad , \tag{55}$$

and an axial spatial correlation

$$\overline{u(x)u(x+s)} = u_o^2 \exp(-s/\Lambda) \quad , \tag{56}$$

which are good approximations to the one-dimensional spectrum and spatial correlation in most shear flows. Here Λ is the longitudinal integral scale, i.e.,

$$\Lambda = \frac{1}{u_o^2} \int_0^\infty \overline{u(x)u(x+s)}\, ds \quad , \tag{57}$$

and u_o is defined by equation (53) above.

From equation (50) and our choice for J (equation (60)), u_o corresponds to the maximum value for $u' \left(\equiv \overline{u^2}^{\frac{1}{2}}\right)$. In the laboratory data this is, approximately,

$$\frac{u_m}{U_m} = .32, \tag{58}$$

where $u_m \equiv \max(u')$. We choose Λ to match the corresponding integral scale in the data. This is, approximately,

$$\frac{\Lambda}{r_m} = .58 \, . \tag{59}$$

There is considerable error involved in the estimation of Λ from the laboratory data (as much as $0.3\, r_m$). Since the proper turbulent length scale is of considerable importance in the dynamics of the flow, this error could have a significant impact on our results. With the choice of u_o and Λ, our spectrum is completely defined.

To choose $J(r)$ we match our initial radial profile for the axial turbulent intensity with the data. A functional form for J which gives a fairly close match is

$$J(r) = \exp\left(-r^2/r_J^2\right), \tag{60}$$

with $\frac{r_J}{r_m} = 2.012$. Figure 7 gives the values for the axial turbulent intensity u' versus radial distance for two different realizations of the ensemble defined above. The solid curve is taken from Pao and Lin (1973). Table 1 gives values for a number of relevant statistical quantities for one realization of the initial flow field.

Although the resulting turbulent velocity field has many of the proper statistical characteristics, it is still lacking in many respects. First of all, because the Fourier modes were chosen to be statistically independent, there is initially not any energy transfer in wave number space. This is exemplified by the low values for the velocity derivative skewness in Table 1, which are a direct measure of this transfer. It has been found, however, that these correlations build up rather rapidly (the velocity derivative skewness attains its proper value by roughly $\frac{\Lambda}{u'} = 0.5$; see e.g., Orszag and Patterson, 1972), and it is not thought that this initial lack of correlation is too severe a limitation. Also, methods have been developed to overcome this (Mehta, 1978). A more critical flaw in the initial field is the approximately zero Reynolds stress $\overline{uw}$. This stress controls both the transfer of turbulent energy from the mean flow, and the diffusion rate of the axial mean velocity. Clearly it is a critical quantity. Similarly, third order moments, e.g., $\overline{u^2 w}$, are also initially approximately zero. These control the self-diffusion of the turbulence. Another more subtle inadequacy in the initialization is the uniformity of the skewnesses and kurtoses. In a wake flow, the values for these quantities are usually larger near the wake edge due to the intermittancy of the flow there. However, the

uniform application of the form function J does not permit this intermittancy. A number of other inadequacies can also be pointed out.

We have understood the nature of the limitations in the initial conditions. We concluded, however, that it would be useful to perform simulations with this scheme because (i) it would determine how significant these limitations were; (ii) it might show us how to better initialize the flow; and (iii) it allowed us to study a flow which ultimately developed in approximately the proper manner. The results to be presented below were obtained using this scheme from Orszag and Pao. We also experimented with several alternative initialization procedures. These alternative methods will be discussed in Section 4.

In order to implement this scheme on the computer we had to finally choose a mesh size, a time step and a viscosity. We chose to treat a cubic box of side length L such that

$$\frac{L}{\mathcal{R}} = 8.0 . \tag{61}$$

This allowed for considerable spread of the wake before boundary effects became important. In wave number space, this resulted in a peak in the three-dimensional spectrum at

$$\kappa_p \mathcal{R} = 2.37 , \tag{62}$$

and a cutoff wave number of

$$\kappa_c \mathcal{R} = 12.64 , \tag{63}$$

which was sufficiently large so that numerical truncation effects were not significant. The time step size Δt was chosen to be

$$\frac{\Delta t \, u'}{\Lambda} = .028 , \tag{64}$$

and the viscosity ν was selected so that the initial turbulent Reynolds number was 50, i.e.,

$$\frac{u'\lambda}{\nu} = 50. \tag{65}$$

This is about the largest value that can accurately be treated on a 32 x 32 x 33 mesh.

3. Numerical Results

In this section we give the results of our direct numerical simulations of the axisymmetric, turbulent wake of a towed body. As mentioned in the previous section, we use the data of Pao and Lin (1973) at $x/D = 36$, which is in the self-similar decay region, to initialize our calculations. We present the results of the simulations of two independent realizations, generated using different random number seeds in the initialization process. The combined results show both the capabilities of the numerical simulations to treat turbulent wakes, as well as provide an estimate of the statistical scatter in the results. We show first some constant contour plots of the instantaneous velocity and vorticity fields to help give a qualitative picture of the wake evolution. We then present plots of the decay of characteristic velocity and length scales, as well as total energies, with time. Finally, we present radial plots of various statistical quantities, and establish the degree to which the self-similar decay is modeled.

3.1 Contour Plots

Although statistical results are necessary to determine the capabilities of the simulations, it is useful to examine contour plots to see qualitatively the development of various features in the flow field. Figures 8 and 9 are contour plots of the longitudinal velocity fluctuation (u) and the magnitude of the fluctuating vorticity $(\omega = \sqrt{\omega_i \omega_i})$ respectively, in a typical plane perpendicular to the mean motion $(x \text{ or } x_1)$, at time zero. The vorticity plot especially shows the localization of the turbulence in the cylindrical region in the center. Note the axisymmetry of the vorticity field, as well as the manner in which it goes rather smoothly to zero with radial distance. These are both a result of the use of the smooth form function in the initialization. Figures 10 and 11 are contour plots of u and ω in a plane parallel to and passing through the x_1 axis, at time zero. Again note the lack of bulges and other nonuniformities at the wake edge, especially in the vorticity field. Also, there appears to be no directional preference in the contours. This reflects the fact that the Reynolds stresses are initially approximately zero.

Figures 12 and 13 are similar contour plots of u and ω in the plane perpendicular to the x_1 axis at nondimensional time T ($\equiv \frac{t\mathcal{U}}{\mathcal{R}}$) of 7.73 , which is one-third of the way through the calculation*. The wake has grown somewhat, and the boundary has become much more convoluted. Also, some of the smaller scale features have been lost to molecular viscosity. Figures 14 and 15 are contour plots of u and ω in the x_1x_2 plane through the x_1 axis at $T = 7.73$. Again note the convoluted nature of the wake boundary, and the growth of the wake. It is also apparent that the velocity field has developed a directional orientation. In the upper-half-plane, the constant contours tend to be oriented with their major axes in the second and fourth quadrants, whereas in the lower half-plane the contours are oriented with their major axes in the first and third quadrants. This can be shown to correspond to a positive Reynolds stress in the upper-half-plane and a negative stress in the lower-half-plane. Note that the mean velocity is positive in the direction of increasing x_1 . The mean velocity gradient has kinematically distorted the initially isotropic-like field into one which has directional preferences.

Figures 16 and 17 are contour plots of u and ω in the x_2x_3 plane at time $T = 15.46$, two-thirds of the way through our calculation. The continual growth of the wake, distortion of the wake boundary, and loss of small scale can again be observed. Figures 18 and 19 give similar plots in the x_1x_2 plane for this time. Again note the increasingly convoluted surface, and the directional preference in the contour lines. The extent of convolution of the boundary regions of the wake will show up as increased values of the velocity (and velocity derivative) skewness and kurtosis in those regions.

3.2 Temporal Behavior

We next turn our attention to the temporal behavior of characteristic velocity and length scales, and of the total energy. In Section 2.3 we found that, in the self-preserving region, characteristic velocities

---

* We define the (constant) velocity $\mathcal{U}$ to be U_m at time zero, and we define $\mathcal{R}$ to be r_m at time zero.

should decay as $t^{-2/3}$, characteristic lengths should grow as $t^{1/3}$, and both the total mean and turbulent kinetic energies decay as $t^{-2/3}$.

In particular this implies that

$$\frac{U_m}{\mathcal{U}} = C_U (t - t_o)^{-2/3} \tag{66}$$

$$\frac{u_m}{\mathcal{U}} = C_u (t - t_o)^{-2/3} \tag{67}$$

$$\frac{r_m}{\mathcal{R}} = C_m (t - t_o)^{1/3} \tag{68}$$

$$\frac{r_T}{\mathcal{R}} = C_T (t - t_o)^{1/3} \tag{69}$$

$$\frac{E}{E_o} = C_E (t - t_o)^{-2/3} \tag{70}$$

$$\frac{e}{E_o} = C_e (t - t_o)^{-2/3} . \tag{71}$$

Here, U_m is the maximum value of the mean velocity deficit, u_m is the maximum value of the longitudinal rms velocity, r_m is the half-radius of the mean velocity, r_T is the half-radius of the longitudinal component of the turbulent intensity, E is the total (integrated) mean flow kinetic energy, E_o is E at time zero, e is the total turbulent kinetic energy, t_o is a virtual origin in time, and C_U, C_u, C_m, C_T, C_E, and C_e are constants. We will look for corresponding behavior in our simulations.

Figure 20 is a plot of the temporal behavior of U_m and u_m for the two different realizations*. Consider U_m first. Initially, the decay rate of U_m is less than predicted by theory, or observed in the data. The dynamic equation for U is equation (32):

$$\frac{\partial}{\partial t} U + \frac{1}{r} \frac{\partial}{\partial r} \left(r \overline{uw} \right) = \nu \frac{1}{r} \frac{\partial}{\partial r} \left(r \frac{\partial}{\partial r} U \right) . \tag{32}$$

---

*In presenting the simulation results, we show the horizontal axis in terms of both x/D (as in Pao and Lin), and also the nondimensional time $T = \frac{t\mathcal{U}}{\mathcal{R}}$. $T = 0$ corresponds to $x/D = 36$, and $T = T_o = -3.76$ corresponds to $x/D = 0$.

The second term on the LHS represents the radial diffusion of mean momentum due to the Reynolds stress $\overline{uw}$. The term on the RHS is the molecular diffusion term, and is small in this case. Initially, the mean velocity peak does not decay since $\overline{uw} = 0$. The Reynolds stress builds up rapidly, however, and by $x/D = 90$, U_m is approximately following the $t^{-2/3}$ behavior for both realizations. Note that there is some difference in the results for the two realizations.

The behavior of u_m is similar. The equation satisfied by $\frac{\overline{u^2}}{2}$ is equation (34):

$$\frac{\partial}{\partial t}\frac{\overline{u^2}}{2} + \overline{uw}\frac{\partial}{\partial r}U + \frac{1}{r}\frac{\partial}{\partial r}\left(r\frac{\overline{u^2 w}}{2}\right) = -\frac{1}{\rho}\overline{u\frac{\partial}{\partial x}p} + \nu\frac{1}{r}\frac{\partial}{\partial r}\left(r\frac{\partial}{\partial r}\left(\frac{\overline{u^2}}{2}\right)\right) - \nu\left[\overline{\left(\frac{\partial u}{\partial r}\right)^2} + \frac{1}{r^2}\overline{\left(\frac{\partial u}{\partial \theta}\right)^2} + \overline{\left(\frac{\partial u}{\partial x}\right)^2}\right]. \tag{34}$$

The dynamics of u' are governed by a complex balance between energy feed from the mean flow $\left(\overline{uw}\frac{\partial U}{\partial r}\right)$, the diffusion of u' by turbulence $\left[\frac{1}{r}\frac{\partial}{\partial r}\left(r\frac{\overline{u^2}}{2}w\right)\right]$, the redistribution of u' between w' and v' $\left(-\frac{1}{\rho}u\frac{\overline{\partial p}}{\partial x}\right)$, and the viscous dissipation of u'. Initially the generation terms and diffusion terms are both zero, due to the initialization scheme. Also, the dissipation is weak due to the initial lack of wave number amplitude correlations. (Hence, the wave number energy transfer is small, which is reflected, for example, in low values of the velocity derivative skewness.) However, by x/D of about 110, these effects all appear to have built up, and u_m decays at roughly the proper rate for the two realizations. Some idea of the relative error can again be seen by comparing the results for the two realizations.

Figure 21 is a plot of the temporal behavior of r_m and of r_T. Considering first r_m, we see that it displays the same effect as does U_m. Initially it does not grow, but apparently after the Reynolds stress has built up, it increases at approximately the proper rate. The same holds for r_T. Initially there is no growth, but by x/D equal to about 110 it is growing at approximately the right rate in correspondence with the decay of u_m.

Figure 23 contains plots of E and e as functions of time. Multiplying equation (32) by ρU and integrating over the crossplane gives the equation for E, i.e.,

$$\frac{d}{dt}E = 2\pi\rho\int_0^\infty r\,\overline{uw}\,\frac{\partial U}{\partial r}\,dr - 2\pi\rho\nu\int_0^\infty r\left(\frac{\partial U}{\partial r}\right)^2 dr. \tag{72}$$

The first term on the RHS represents the loss of mean kinetic energy to turbulence, while the second term is the molecular dissipation term, which is small. Mean flow energy is lost to the turbulence through the action of the Reynolds stress $\overline{uw}$ on the mean velocity gradient. The decay of E has established close to its proper behavior by about $x/D = 100$. The equation for e is obtained by integrating the sum of equation (38) and its counterparts for $\overline{w^2}$ and $\overline{v^2}$, and is

$$\frac{d}{dt}e = -2\pi\rho\int_0^\infty r\,\overline{uw}\,\frac{\partial U}{\partial r}\,dr - \varepsilon, \tag{73}$$

where ε is the viscous dissipation. Thus the time rate of change of e is a balance between energy feed from mean flow and viscous dissipation. Again, the proper decay rate is approximately obtained by x/D about 110. The slightly slower decay rate could be due to wall effects, statistical scatter, the lack of sub-grid scale model, or an erroneous value for the initial integral scale Λ.

Although the approximate proper decay rate has been attained by these quantities, their ratios have changed from the initial conditions. From Pao and Lin (1973) at $x/D = 36$,

$$\frac{u_m}{U_m} = .32, \quad \frac{r_T}{r_m} = 2.0, \tag{74}$$

and these ratios are maintained throughout the self-similar region. In our simulations, however, although we started the values of the above ratios properly (to within statistical scatter), the values in the self-similar range became

$$\frac{u_m}{U_m} = .47, \quad \frac{r_T}{r_m} = 1.66. \tag{75}$$

These values are somewhat different from the data, and are another reflection of our inadequate method of initialization. These ratios do vary, however, for different shaped obstacles. Our wake may be more representative of the wake of a sphere than a slender body.

To summarize, initially the time development of the flow does not correspond to the self-similarity theory and the data due to inadequate initialization, especially of the Reynolds stress. After the flow has adjusted, however, and the Reynolds stresses have built up, these quantities develop in time at approximately the proper self-similar rate, over a distance of about 100 to 270 diameters (or a time of $23.2\frac{R}{U}$. In the meantime the ratios $\frac{u_m}{U_m}$ and $\frac{r_T}{r_m}$ change from their initial values, so that our calculations may be more representative of the wake of a different body than that used by Pao and Lin.

3.3 Spatial Behavior

In this section we present the radial distribution of various statistical quantities for different decay times. Self-similarity theory predicts that if the velocities are normalized by U_m (or u_m), and the lengths are scaled by r_m (or r_T), then the radial distribution of a particular statistical quantity, say $\frac{1}{U_m} U(\frac{r}{r_m})$, should collapse for different times. The ability of this scaling to collapse the data, and the degree to which the resulting profiles agree with corresponding profiles from laboratory data is a good check of the capability of the numerical simulations to correctly model the physical processes occurring in the wake.

To obtain the appropriate velocity and length scales, we assume that the flow is self-similar, and subjectively estimate best fits to the data given in Figures 20 and 21. The results are

$$\frac{U_m^*}{\mathcal{U}} = 15.8 \left(\frac{x}{D}\right)^{-2/3} \tag{76}$$

$$\frac{u_m^*}{\mathcal{U}} = 7.5 \left(\frac{x}{D}\right)^{-2/3} \tag{77}$$

$$\frac{r_m^*}{\mathcal{R}} = .26 \left(\frac{x}{D}\right)^{1/3} \tag{78}$$

$$\frac{r_T^*}{\mathcal{R}} = .44 \left(\frac{x}{D}\right)^{1/3} \tag{79}$$

(The notation $(\,)^*$ indicates a best estimate of the self-similar decay law for the numerical data.) These expressions are given by the solid curves in Figures 20 and 21. The following data are scaled using these expressions to compute the appropriate scaling quantity at the particular x/D .

Figure 23 gives data from the first realization (R1) for $\frac{U}{U_m^*}$ versus $\frac{r}{r_m^*}$ for the locations $x/D = 150$, 205, and 260 ; U_m decreases by about 30 percent and r_m increases by 20 percent over this range. We see, first of all, that the scaling collapses the data very well, except near the origin, where the statistical scatter is expected to be the greatest. The laboratory results tend to follow the self-similar result rather well (Figure 6), although the scatter is fairly large for $\frac{r}{r_m} > 1.5$, so that it is difficult to conclude that the agreement is good in this region. Previous measurements of the wakes of two-dimensional bodies (see, e.g., Townsend, 1976) have consistently shown that the theory predicts somewhat larger values than are observed for $\frac{r}{r_m} > 1.5$. This is usually attributed to decreased turbulent diffusion near the wake edge, due to the intermittent nature of the flow there. We see that the simulation results tend to be slightly low for small $\frac{r}{r_m^*}$. This

is due to the fact that both realizations were taken into account in the normalization. Data from the second realization lie slightly above the theoretical curve in this same region (Figure 24). The simulation results also lie below the theoretical curve for $\frac{r}{r_m^*} > 1.5$. The fact that U_m initially started as an exact fit to the similarity result may indicate that the numerical simulations have added a realistic feature.

Figure 24 is a plot of the same quantity at the same locations for the second realization (R2). Again, the collapse is fairly good. The high values for small $\frac{r}{r_m^*}$ indicates the data scatter to be expected from one realization to another. The results for $\frac{r}{r_m^*} > 0.7$ are in good agreement with those from R1 . We conclude from these results that the mean velocity behaves in a manner very close to the laboratory data, but that there is some scatter in the data near the origin.

Figure 25 is a plot of $\frac{u'}{u_m^*}$ versus $\frac{r}{r_m}$ for the downstream locations $x/D = 150$, 205, and 260 for R1 . The dashed line is a rough fit of the laboratory data of Pao and Lin (1973). The laboratory data curve has been compressed so that $\frac{r_T}{r_m}$ for the data takes on the same value given by equation (75) instead of (74) i.e., 1.66. By plotting all the data versus $\frac{r}{r_m^*}$, we can compare the simulation results with laboratory data, and simultaneously compare u' with U and other variables. The collapse of the simulation data is again fairly good. The scatter in the data for u' is expected to be significantly larger than that for U because the sampling error increases monotonically with the order of the statistical quantity (see, e.g., Kenney, 1954). For the choice of u_m^* and r_m^* given by equations (77) and (78) the agreement with the laboratory data is only fair. If this data were matched independent of R2 , a better fit could be obtained.

Figure 26 is a similar plot for R2 . Again the collapse of the data is fairly good except near the origin. This realization agrees much better with the laboratory data than the first realization. This

is partly due to the choice of u_m^* and r_m^*. When the data for $\frac{u'}{u_m^*}$ are superimposed for the two realizations, distinct differences in the two sets can be noted. This gives some idea of the magnitude in the scatter in the data to be expected in the simulation.

Figure 27 is a plot of the normalized Reynolds stress $\frac{\overline{uw}}{u_m^{*2}}$ versus $\frac{r}{r_m^*}$ for $x/D = 150$, 205, and 260 in R1. The solid curve gives the prediction of the similarity theory, equation (31), and the hatched lines gives the data of Pao and Lin (1973). The collapse is fairly good considering the error expected in computing the Reynolds stress. Furthermore, the agreement with the laboratory data is reasonable. In Figure 28 we present similar data from R2. In this realization, the collapse is not quite as good. Also, a possible trend appears to be in the data, with the peak value increasing with x/D. Superimposing the two sets of data for the two realizations shows reasonable agreement between the two.

Figure 29 is a plot of $\frac{\overline{u^2 w}}{u_m^{*3}}$ versus $\frac{r}{r_m^*}$ for $x/D = 150$, 205, and 260 for R1. The radial flux of $\overline{u^2}$ is represented by $\overline{u^2 w}$ and is an essential part of the dynamics of $\overline{u^2}$ (see equation (38)). The collapse is reasonable, except near the origin where the scatter in the data is expected to be greatest. Although we presently do not know of data with which to compare the result, we see that it has at least the proper qualitative behavior; $\overline{u^2}$ is being diffused by the turbulence away from its peak (which occurs at about $\frac{r}{r_m^*} \approx 1$, Figure 25), towards the origin for $\frac{r}{r_m^*} \lesssim 0.9$, and away from the origin for $\frac{r}{r_m^*} \gtrsim 0.9$. Figure 30 gives the same data for R2. Here the collapse is not nearly as good. Apparently this quantity has not fully adjusted in this range. Some of the scatter in the results could also be due to poor statistics.

The intermittancy of the wake turbulence is reflected in the flatness factor of the velocity field. Townsend (1949) has shown for wakes, and Wygnanski and Fiedler (1970) for mixing layers, that the velocity kurtosis is approximately equal to the inverse of the intermittancy factor. Figure 31 is a plot of the radial distribution of the velocity

kurtosis for R1 and the same three downstream locations. At the start of the calculation, the profile is flat (Table 1), due to the method of initialization, indicating there is no intermittancy in the flow. As the wake develops, however, the outer regions of the wake become highly contorted (e.g., Figures 8 to 19), and the velocity becomes highly intermittant, which is reflected in the sharp increase in the kurtosis at the wake edge. The dashed line is a rough fit of the data of Pao and Lin (1973), and the agreement between the simulations and laboratory data is reasonable.

Figure 32 is the same plot for R2 . While the collapse of the data is good, the agreement with the laboratory data and with R1 is poor, especially in the locations of the peak value. Apparently in R2 the wake edge is neither as contorted nor as far out as in R1 . This again is an indication of the deviations to expect from one realization to another. To compute the kurtosis accurately, we may need to compute several realizations and use ensemble averaging.

The velocity skewness is also an indicator of the intermittancy of the flow field. Figure 33 is a plot for the velocity skewness for R1 for the same three downstream locations. Again the collapse is fairly good, and the wake edge is clearly distinguishable through the large skewness values. The agreement with the laboratory data is reasonably good. Figure 34 gives the same plot for R2 . The results are not in good agreement with either the laboratory data or with the skewness data from R1 . This is another indication that the wake edges for the two realizations are in different radial locations.

To summarize the radial plots, in general the collapse of the data using the self-similarity scaling is very good. Also the agreement with laboratory data is generally good, except for two cases. The first is the turbulence intensity (u') profile, where the ratio $\frac{r_T}{r_m}$ has changed from its initial value, equations (74) and (75). However, when u' is plotted against $\frac{r}{r_T^*}$, or, equivalently, when the ratio of $\frac{r_T}{r_m}$ given by (75) is used to plot the laboratory data, the agreement is then fairly good. Secondly, some significant differences were observed in the skewness and kurtosis for the second realization.

4. Other Methods of Initialization

It is obvious from the simulation results presented that our method of initialization, although properly treating many important turbulence properties, was inadequate to properly initialize all of the significant turbulence quantities in the wake. This inadequacy was particularly exhibited in the initial Reynolds stresses, higher order flux terms, and skewnesses and kurtoses.

We have begun a preliminary exploration of ways to improve our initialization procedure. Although we have not yet had time to reach definite conclusions on better ways to initialize the turbulence in the wake, we thought it would still be useful to discuss the results of these efforts. For the successful utilization of direct numerical simulations of turbulence, the difficulties inherent in properly initializing turbulent shear flows may be as important to resolve as the questions arising from subgrid-scale modeling.

We think that the key improvements to be made are in the proper initialization of the Reynolds stresses and higher order flux terms, such as the turbulent flux of turbulent energy. As mentioned in the last section, these terms represent the diffusion of the mean velocity by the turbulence, the generation of turbulent energy, and the self-diffusion of the turbulence. Improper initialization eliminates the possibility of an exact initialization of the wake. A secondary improvement of importance is the correct specification of the structure of the flow at the wake edge, which is reflected in the skewnesses and kurtoses.

A possible method to treat these problems is the extension of a technique used by Rogallo (1977) and Mehta (1978) in computing homogeneous turbulence decay. As our calculations proceed in time, the Reynolds stresses and higher moments do build up to approximately their proper values. During this buildup period, however, the mean velocity has diffused outward and the turbulence has decayed somewhat, so that all of the proper conditions are not attained. The idea is to reinitialize the velocity field by retaining the phase relationship in each Fourier mode that has been attained when the stresses have built up, but reimposing the initial Fourier amplitude. Since the information about the Reynolds stresses and higher movements is mainly contained in the

phase relationships of the modes, it was hoped that the initial Reynolds stress behavior would be desired. Because the energy levels were readjusted to their initial values, it was also hoped that the initial profiles of turbulence intensity would again take on their proper values.

We implemented this technique on the computer. Two free parameters at our disposal were the number of time steps between reimposing the initial Fourier amplitudes (N_τ), and the number of times we reimpose the initial amplitudes (N). It takes about 100 time steps for the Reynolds stress to attain its proper value. We experimented with the following values of N_τ and N: $(N, N_\tau) = (1, 120), (1, 80), (2, 40), (5, 20), (10, 10)$. In general, we found that the best overall results were obtained for cases with smaller N. We will present the results for $(N, N_\tau) = (2, 40)$ which is representative of the better results, but which also points out some of the difficulties with the method.

Figure 35 contains a plot of the initial profile of the longitudinal turbulent intensity u' before the field was reinitialized. Figure 36 contains a plot of the corresponding Reynolds stress $\overline{uw}$. The turbulent field for this realization was reinitialized using values of $N = 2$ and $N_\tau = 40$. The reinitialized quantities are also shown in Figures 35 and 36. The new Reynolds stress has developed to the proper form, although its peak value is somewhat larger than the corresponding value in the laboratory data. The difference is typical of the statistical fluctuations that we have seen in $\overline{uw}$ in our simulations (Figures 27 and 28). The new turbulence intensity profile has changed substantially from the initial profile. Some of the energy near the axis has moved to outside the wake. Apparently, although the proper phase information for the Reynolds stress has been retained, the phase information necessary to maintain the proper profile for u' has been degraded. Because of this behavior, we find this method as presently used unacceptable, and are working on its improvement.

We have also experimented with several other methods. The first is a shooting method, which takes into account the fact that, although the conditions ultimately attained are not exactly as desired (e.g., $\frac{u_m}{U_m} = 0.47$ instead of 0.32), they are close. Thus it may be possible to adjust the initial field to shoot to the proper values for these quantities.

We have implemented this shooting method and are presently testing it. Another method, suggested by Moin (1978), involves the use of the eigenfunctions of the most unstable modes for the wake stability problem. The idea is that the flow structure which supports the Reynolds stresses may be similar to these unstable modes. Their Reynolds stress can be easily computed, and the eigenfunctions added into our initial field to produce the proper stresses. We have yet to implement this method.

Several other ideas are under consideration. We are still in the process of studying the applicability of these various methods, with the ultimate goal of the proper initialization of the turbulence field.

5. Conclusions

From the numerical simulation data presented in the preceeding section, we can draw a number of conclusions about the capabilities of the direct numerical simulations of turbulence. In general, the agreement of the numerical simulation results with the laboratory data and the self-similarity theory was good. In terms of the temporal behavior of the simulated flow over a span of time of about $15\frac{R}{U}$,

(i) the maximum mean and turbulent velocities decayed at approximately the proper rate $((x/D)^{-2/3})$;

(ii) both the mean and turbulent wake radii increased at approximately the proper rate $((x/D)^{-1/3})$;

(iii) the total integrated mean and turbulent energies decayed at approximately the proper rate $((x/D)^{-2/3})$.

Furthermore, over this same interval of time, using self-similarity scaling, we were able to obtain reasonably good collapse, and also reasonable agreement with laboratory data, for

(i) the mean velocity profile

(ii) the turbulent intensity profile

(iii) the Reynolds stress profile

(iv) the profile for $\overline{u^2 w}$ (no laboratory data was available), and

(v) the profiles for skewness and kurtosis.

In addition, several realistic features, which were not in our initial conditions, subsequently appeared later in time in the numerical simulations. These include

(i) the development and maintenance of the Reynolds stress,

(ii) the development and maintenance of higher order correlations, e.g., $\overline{u^2 w}$;

(iii) the development of intermittency near the wake edge, which qualitatively shows up as bulges in the wake, and is reflected by the development of the skewness and kurtosis to reasonable values.

It also appeared that a subgrid-scale model is not a primary necessity for computing this free shear flow, although a subgrid-scale model may prove to be necessary in the future when more careful comparisons with data, especially for the decay of turbulent energy, are made.

The comparisons were hampered by two inadequacies in the present calculations. The first was the initialization process. The turbulent field, especially in terms of the Reynolds stresses, was not adequately initialized, which limited the conclusions that we could draw concerning numerical simulations. Secondly, there was a significant amount of scatter in our data, both in an individual realization, and from one realization to another.

Given these limitations, the present work greatly increases our confidence in the capabilities of direct numerical simulations to accurately treat the physics of turbulent shear flows. The turbulence in the axisymmetric wake is governed by a complex balance among the following mechanisms: generation of energy from the mean flow, diffusion of turbulence radially by the turbulence, intercomponent transfer of energy, and dissipation. All of these processes have to be represented faithfully for the resulting statistics to possess the proper behavior. (It should be noted that there are no adjustable constants in

our simulations.) Thus we feel that the outlook is good for using direct numerical simulations to predict statistical results which depend on the large-scale features of free turbulent shear flows.

From our work, the emphasis for future research work in this field has become more clear. The following are topics which we think should be addressed in the near future:

(i) The method of initialization should be improved to include the proper initialization of the Reynold stress and higher order moments. Until this is done close comparisons with data will be difficult. (The initialization of the turbulent velocity field for a statistically time dependent problem is analogous to the specification of turbulent inflow boundary conditions for spatially nonhomogeneous problems.)

(ii) The present simulations should be examined in more depth to look, for example, at the behavior of spectra and correlations. At the same time, the effects of a subgrid-scale model should be examined.

(iii) Because of the limitations in statistics obtained from these 32 x 32 x 33 grid calculations, it is probably necessary to use a 64 x 64 x 65 grid and/or compute a number of realizations in order to obtain statistics which will adequately test the method.

(iv) It is important to develop techniques for specifying proper inflow and outflow boundary conditions to enable the treatment of more general problems.

References

Batchelor, G. K. (1967) Fluid Dynamics, Cambridge U. Press

Bukreev, V. I., O. F. Vasilev, and Yu. M. Lytkin (1972) Proc. Acad. Sci. USSR, Vo. 207, No. 4, pp. 805-807.

Carmody, T. (1964) ASME J. Basic Engin., Vol. 86, pp. 869-882.

Chevray, R. (1968) ASME J. Basic Engin., Vol. 90, pp. 275-284.

Cooper, R. D. and M. Latzky (1955) The David Taylor Model Basin Report No. 963, October.

Deardorff, J. W. (1970) J. Fluid Mech., Vol. 41, Pt. 2, pp. 453-480.

Deardorff, J. W. (1974) Bound. Layer Met., Vol. 7, pp. 81-106.

Feller, W. (1957) Probability Theory, Vol I, Wiley.

Ferziger, J. H., V. B. Mehta, and W. C. Reynolds (1977) In Symp. on Turb. Shear Flows, Penn. St. U., pp. 14.31-14.40.

Fox, D. G., and S. A. Orszag (1973) J. Comp. Phys., Vol. 11, pp. 612-619.

Grotzbach, G., and V. Schumann (1977) In Symp. on Turb. Shear Flows, Penn. St. U., pp. 14.11-14.20.

Kenney, J. F. (1954) Mathematics of Statistics, Pt. II, Van Nostrom.

Leonard, A. (1974) Adv. in Geophys., Vol. 18A, p. 237.

Lilly, D. K. (1967) In Proc. IBM Sci. Comp. Symp. on Environ. Sci., IBM Form No. 320-1951, p. 195.

Love, M. D., and D. C. Leslie (1977) In Symp. on Turb. Shear Flows, Penn. St. U., pp. 14.1-14.10.

Mansour, N. N., P. Moin, W. C. Reynolds, and J. H. Ferziger (1977) In Symp. on Turb. Shear Flows, Penn. St. U., pp. 14.21-14.30.

McMillan, O. J., and J. H. Ferziger (1978) Direct Testing of Subgrid-Scale Models, NEAR TR 1974, November.

Mehta, V. B. (1978) Private Communication.

Moin, P. (1978) Private Communication.

Moin, P., W. C. Reynolds, and J. H. Ferziger (1978) "Large Eddy Simulation of Incompressible Turbulent Channel Flow," Stanford Thermosciences Div. Report No. TF-12, May.

Orszag, S. A. (1974) "Numerical Simulations of Turbulent Flows," Flow Research Report No. 52, November.

Orszag, S. A. and G. S. Patterson, Jr. (1972) In Statistical Models and Turbulence (ed. M. Rosenblatt and C. Van Atta), p. 127, Springer.

Orszag, S. A., and Y.-H. Pao (1974) Adv. in Geophys., Vol. 18A, pp. 225-236.

Orszag, S. A., and M. Israeli (1974) Ann. Rev. Fluid Mech., Vol. 6, pp. 281-318.

Pao, Y.-H., and J.-T. Lin (1974) Bull. Am. Phys. Soc., 19, pp. 1164-1165.

Rogallo, R. S. (1978) Private Communication.

Roshko, A. (1976) AAIA J., Vol. 14, No. 10, pp. 1349-1357.

Smagorinsky, J., S. Manabe, and J. L. Holloway (1975) Mon. Weath Rev., Vol. 93, p. 727.

Tennekes, H., and J. L. Lumley (1972) A First Course in Turbulence, MIT.

Townsend, A. A. (1949) Proc. Roy. Soc., Vol. 197, Ser. A., p. 124.

Townsend, A. A. (1976) The Structure of Turbulent Shear Flow, Cambridge U. Press.

Uberoi, M. S., and P. Freymuth (1970) Phys. Fl., Vol. 13, pp. 2205-2210.

Wygnanski, I., and H. E. Fiedler (1970) J. Fluid Mech., Vol. 41, Pt, 2, pp. 327-361.

Table 1. Initial Data - Realization 1.

n Cylindrical Annulus	N_n Number of Points	$\frac{1}{\sqrt{N_n}}$	r/r_m (r_m = 0.82815)	U	u' (axial)	w' (radial)	v' (angular)	$\overline{u^2 w}$ ($X10^{-2}$)	$\overline{w^3}$ ($X10^{-2}$)	$\overline{v^2 w}$ ($X10^{-2}$)
1	32	0.1768	0.1185	1.0000	0.3588	0.	0.	0.	0.	0.
2	256	0.0625	0.3556	0.9363	0.3401	0.3714	0.4055	0.8207	0.6609	0.6170
3	512	0.0442	0.5927	0.7866	0.3370	0.3688	0.4054	0.7777	-0.4200	0.1491
4	640	0.0395	0.8298	0.6178	0.3254	0.3624	0.3619	-0.1412	-0.4814	0.5297
5	768	0.0361	1.0669	0.4537	0.3037	0.3525	0.3308	0.0781	-0.0756	0.4250
6	1280	0.0280	1.3040	0.2884	0.2842	0.3113	0.2956	0.1706	0.0645	0.0712
7	1152	0.0295	1.5411	0.1717	0.2748	0.2636	0.2579	0.0835	0.1191	-0.0121
8	1536	0.0255	1.7782	0.0947	0.2046	0.2146	0.2086	0.0322	0.0426	0.0301
9	1792	0.0236	2.0153	0.0462	0.1683	0.1656	0.1719	0.0124	-0.0227	0.0004
10	1792	0.0236	2.2524	0.0212	0.1402	0.1279	0.1386	-0.0135	-0.0226	0.0145
11	2176	0.0214	2.4895	0.0090	0.1035	0.0963	0.1030	-0.0020	-0.0104	0.0119
12	2048	0.0221	2.7266	0.0036	0.0761	0.0728	0.0783	-0.0025	0.0042	0.0036
13	2560	0.0198	2.9637	0.0013	0.0528	0.0529	0.0612	-0.0014	0.0028	-0.0006
14	2944	0.0184	3.2008	0.0004	0.0369	0.0369	0.0450	-0.0004	0.0003	-0.0005
15	2816	0.0188	3.4379	0.0001	0.0285	0.0260	0.0352	-0.0001	0.0000	0.0000
16	3072	0.0180	3.6750	0.0000	0.0218	0.0175	0.0252	0.0000	0.0000	0.0000

Table 1. (Cont.)

$\overline{uw}$ $(X10^{-2})$	$\frac{\overline{u^3}}{\overline{u^2}^{3/2}}$	$\frac{\overline{u^4}}{\overline{u^2}^2}$	$\overline{\left(\frac{\partial u}{\partial x}\right)^2}$	λ	$\frac{\overline{\left(\frac{\partial u}{\partial x}\right)^3}}{\overline{\left(\frac{\partial u}{\partial x}\right)^2}^{3/2}}$	$\frac{\overline{\left(\frac{\partial u}{\partial x}\right)^4}}{\overline{\left(\frac{\partial u}{\partial x}\right)^2}^2}$
0.	-0.4093	2.403	0.8769	0.3832	-0.6699	3.671
0.3364	-0.3380	2.889	1.3641	0.2912	-0.1833	3.065
-0.2297	0.0635	2.963	1.3969	0.2851	0.1643	3.064
-0.8677	0.0330	2.578	1.0226	0.3218	-0.0264	2.862
0.2706	-0.0309	2.735	0.9951	0.3044	-0.0618	3.099
0.3714	0.0617	2.777	0.8276	0.3124	0.0065	2.901
-0.3018	0.2788	2.773	0.5973	0.3207	0.0543	2.756
-0.2593	0.0640	2.971	0.3936	0.3261	0.0315	2.888
0.0085	0.0414	2.853	0.2549	0.3333	-0.0348	2.837
-0.0327	0.0730	3.096	0.1702	0.3398	0.0334	2.936
-0.0066	0.0398	2.988	0.0929	0.3394	-0.0477	2.989
-0.0177	0.2047	3.029	0.0564	0.3204	0.0290	2.947
-0.0053	0.0143	3.006	0.0304	0.3205	-0.0641	2.929
0.0011	0.0410	2.995	0.0167	0.2849	0.0340	2.756
-0.0004	0.0407	3.257	0.0090	0.3007	-0.0478	3.021
-0.0002	-0.0563	3.333	0.0052	0.3026	0.0737	3.093

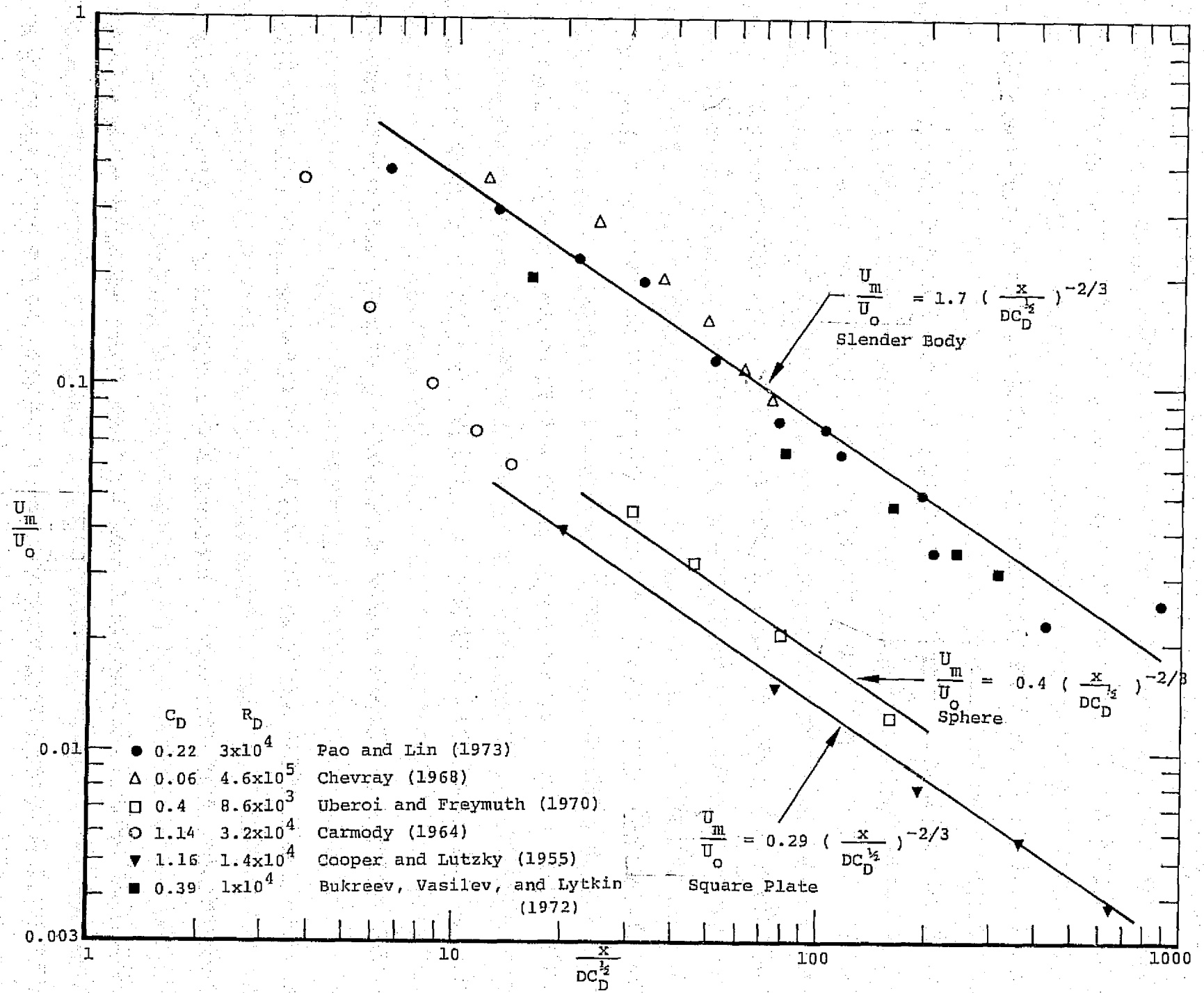

Figure 1. Decay of Maximum Mean Velocity U_m/U_o (From Pao and Lin, 1973).

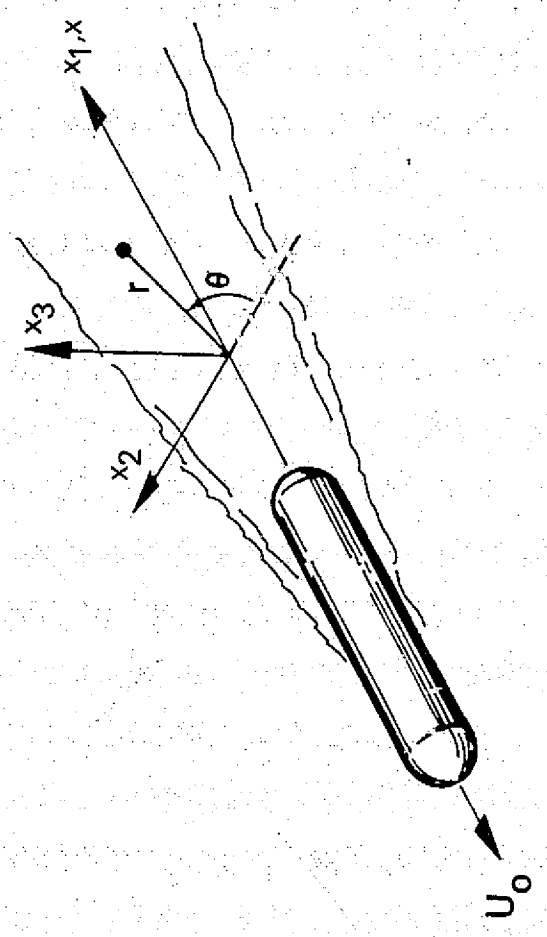

Figure 2. Problem Geometry.

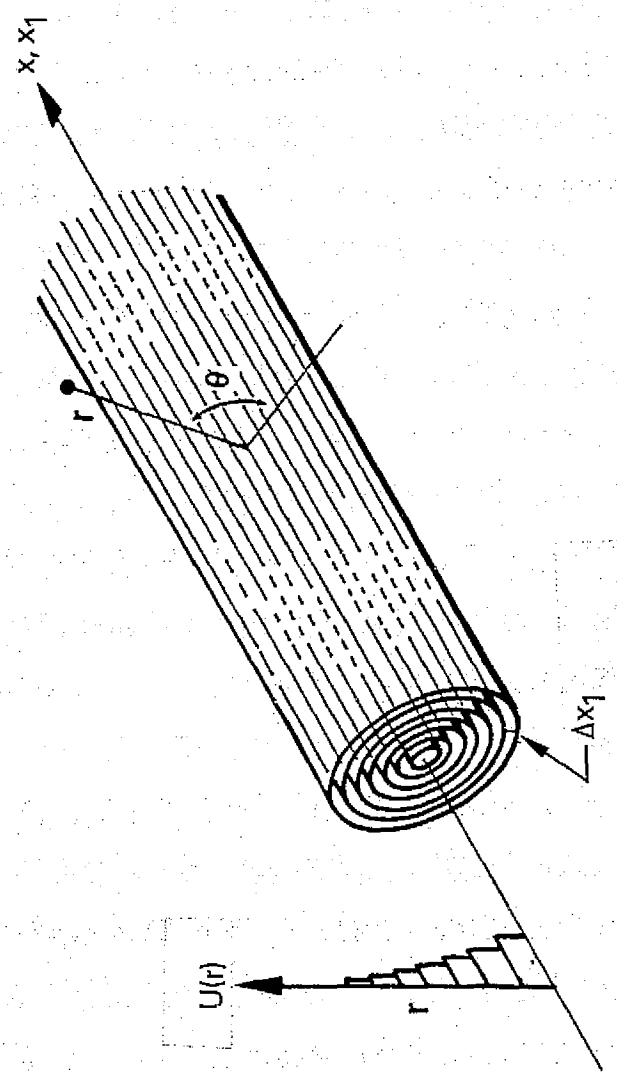

Figure 3. Annuli used to Compute Spatial Averages.

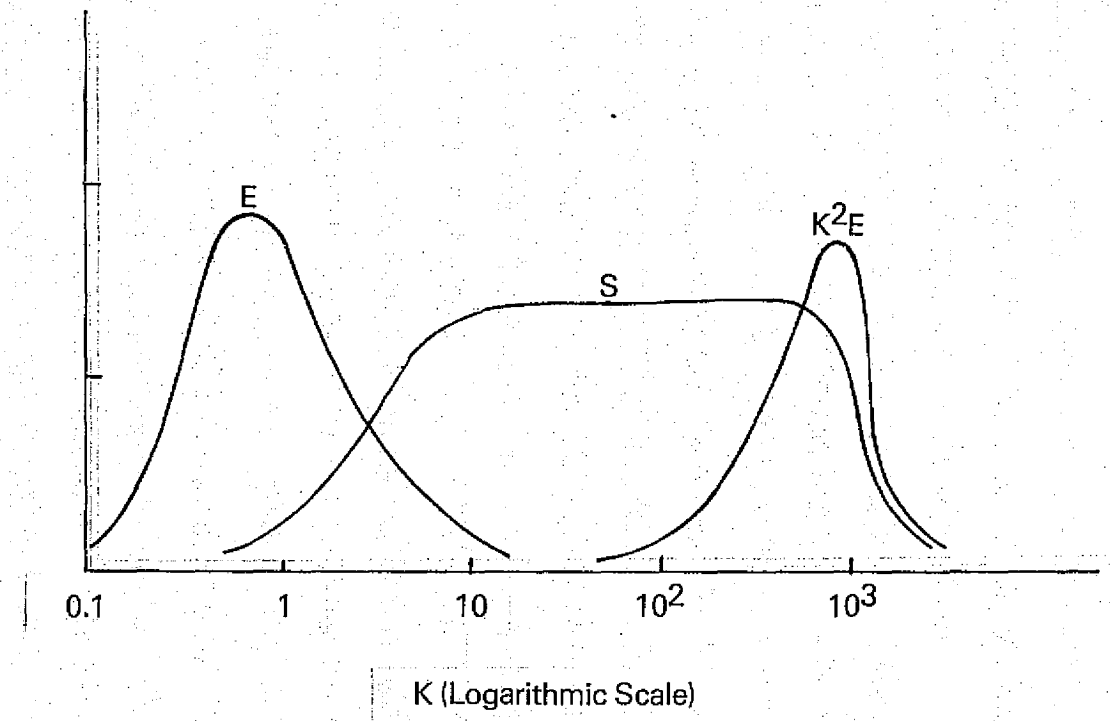

Figure 4. Spectral Distributions of Turbulent Intensity (E), Energy Transfer (S), and Viscous Dissipation (K^2E) at High Reynolds Number (Adapted From Townsend, 1976).

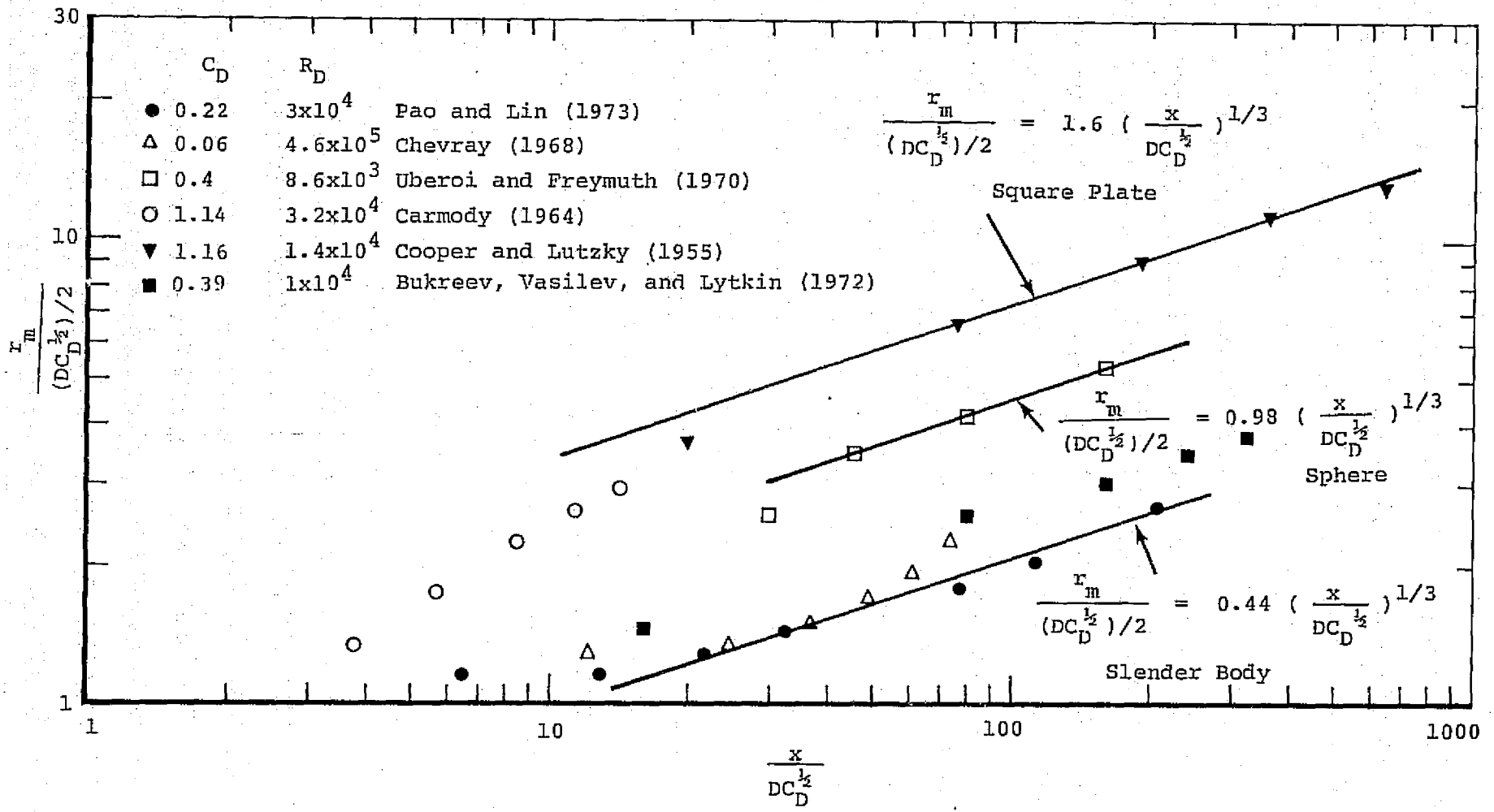

Figure 5. Growth of Mean Wake Radius $r_m/(DC_D^{1/2}/2)$ (From Pao and Lin, 1973).

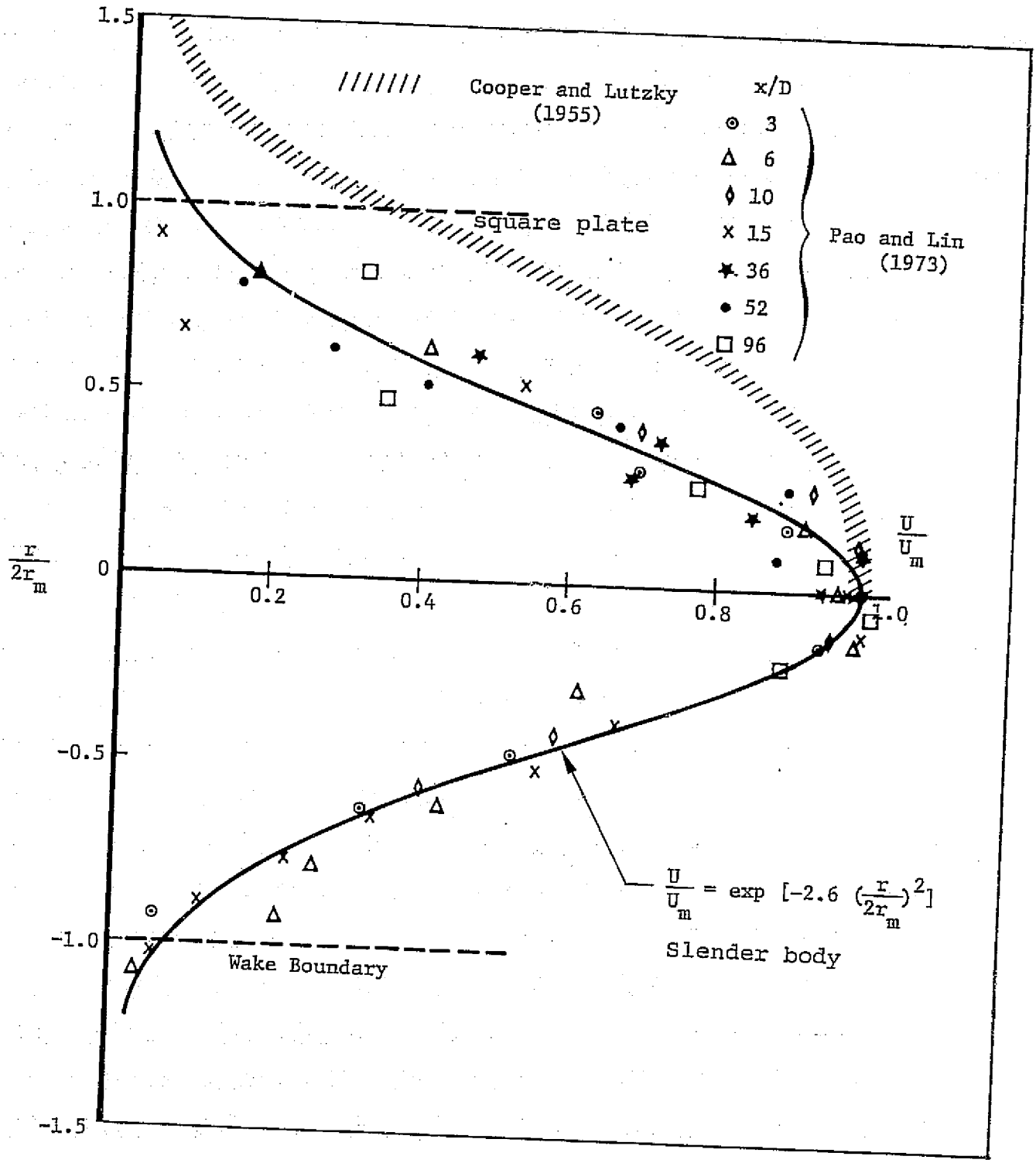

Figure 6. Normalized Profile of Mean Velocity U/U_m (From Pao and Lin, 1973).

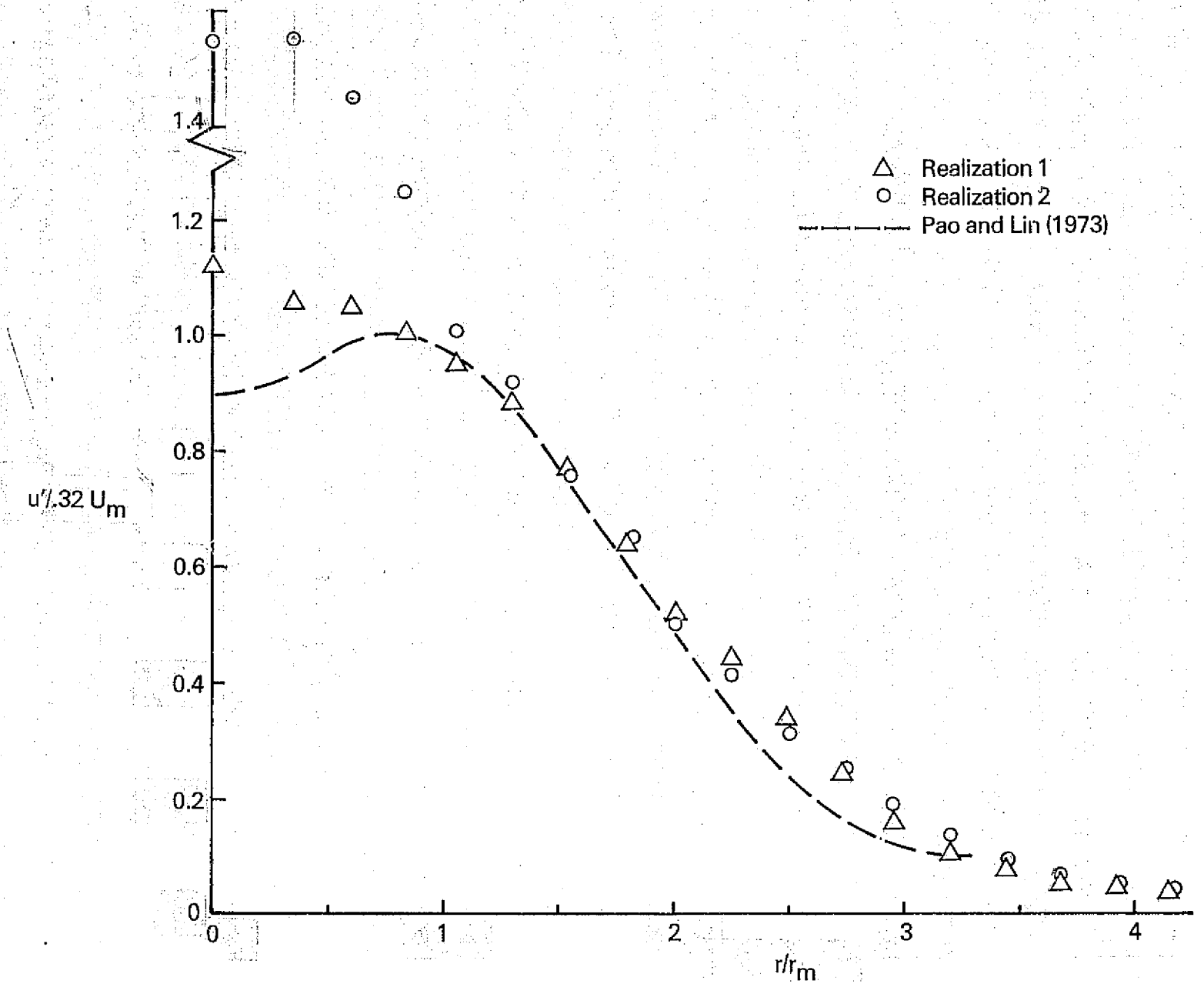

Figure 7. Initial Axial Turbulence Intensity for Two Different Realizations.

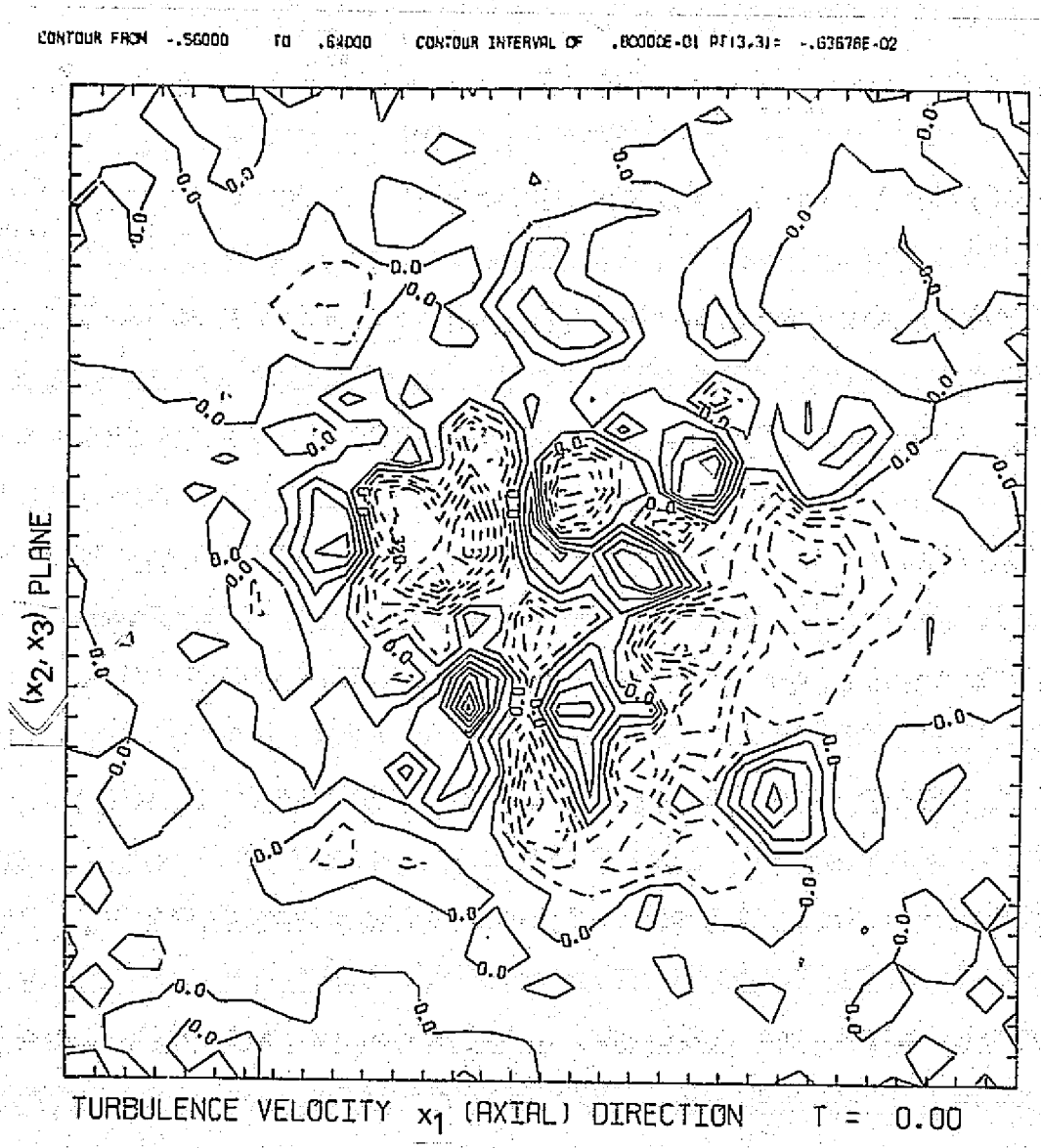

Figure 8. Velocity Field Contour Plot.

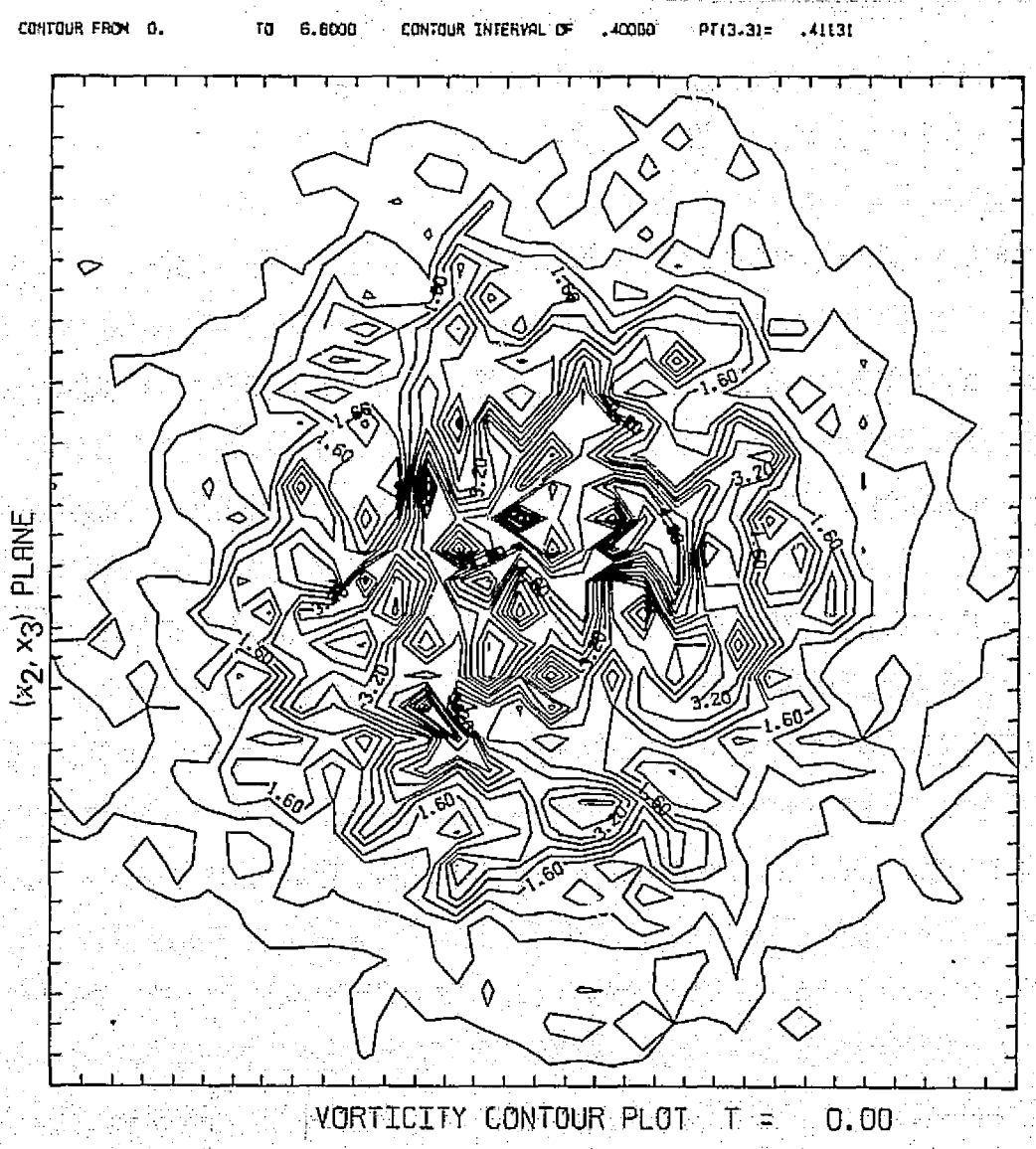

Figure 9. Vorticity Magnitude Contour Plot.

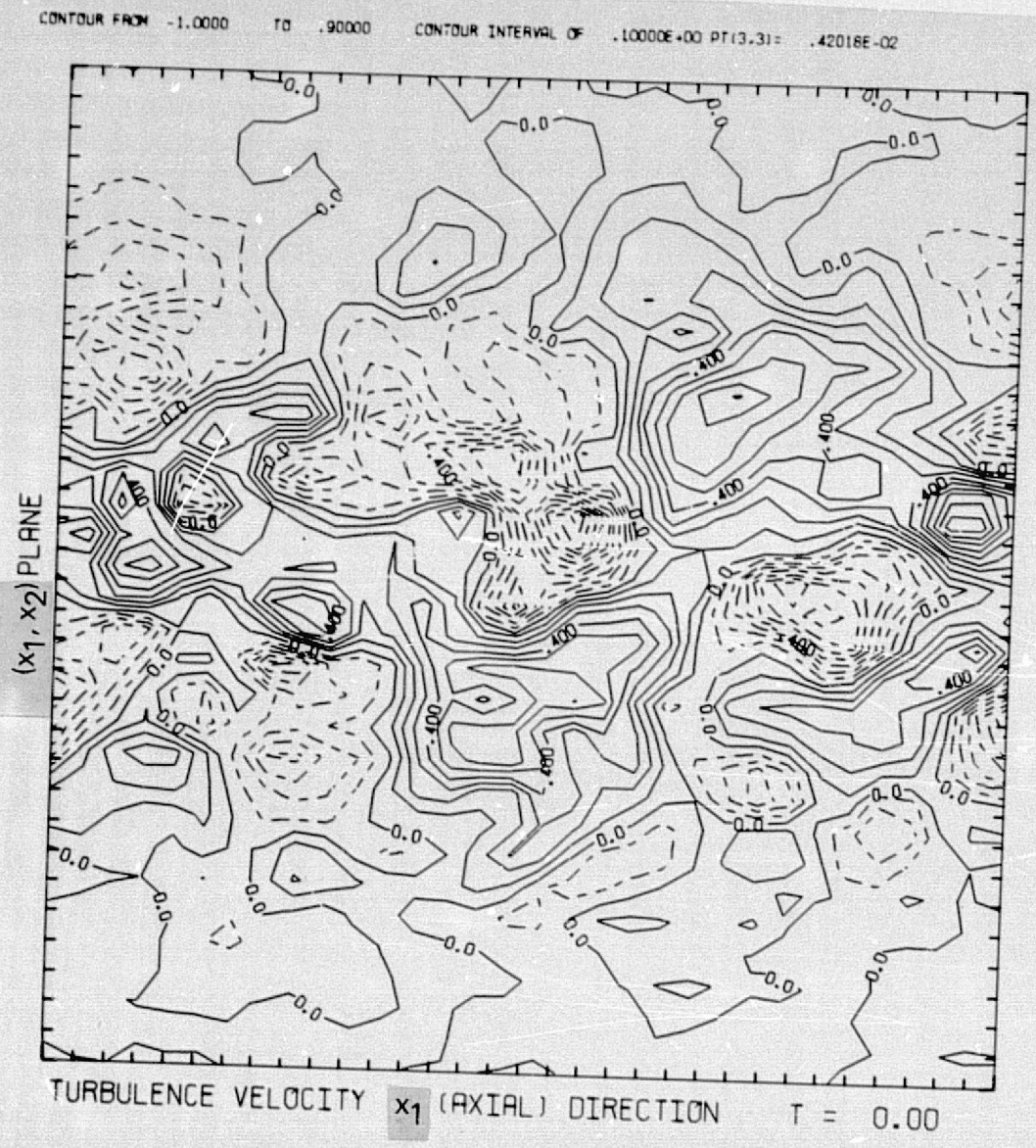

Figure 10. Velocity Field Contour Plot.

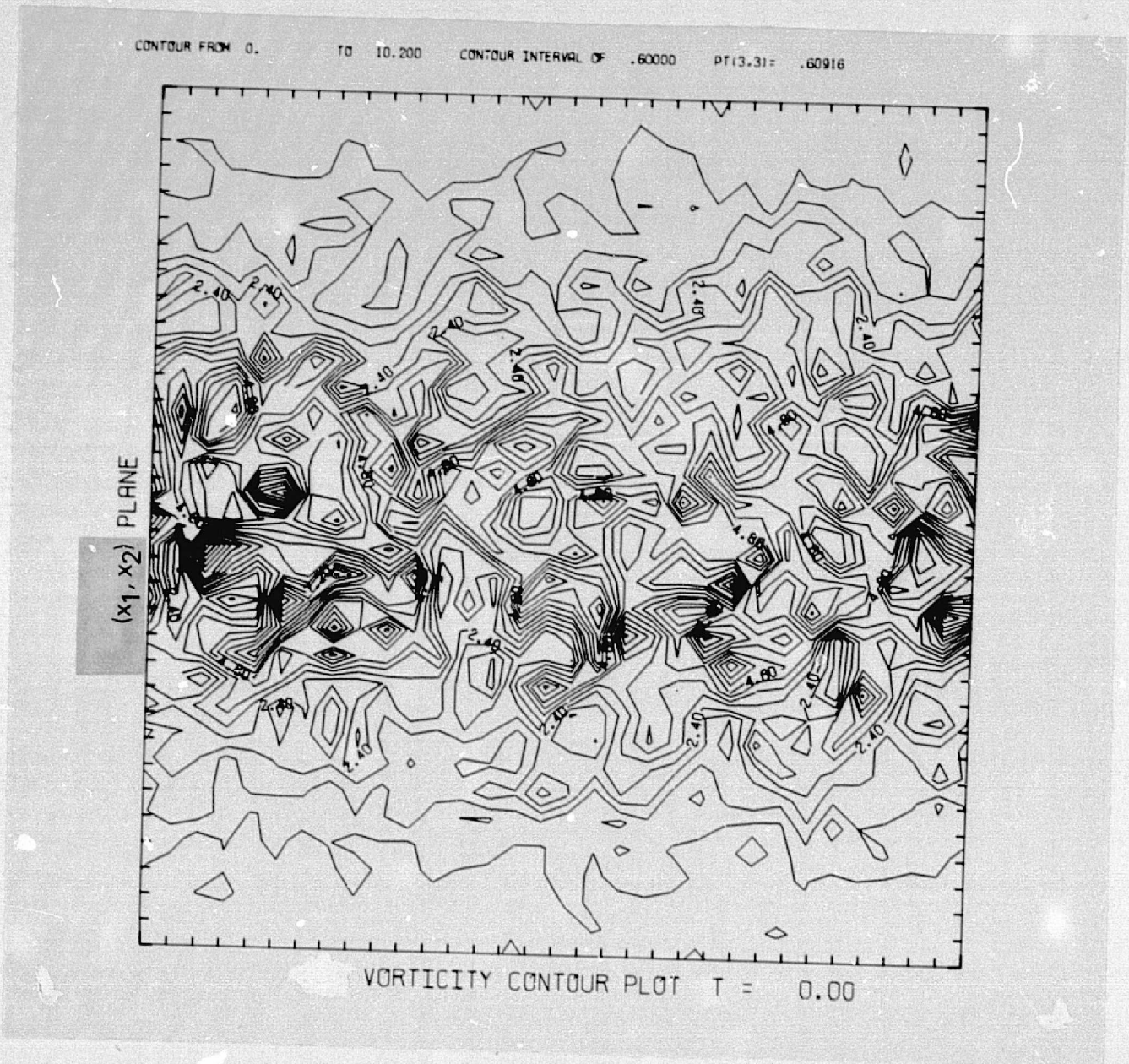

Figure 11. Vorticity Magnitude Contour Plot.

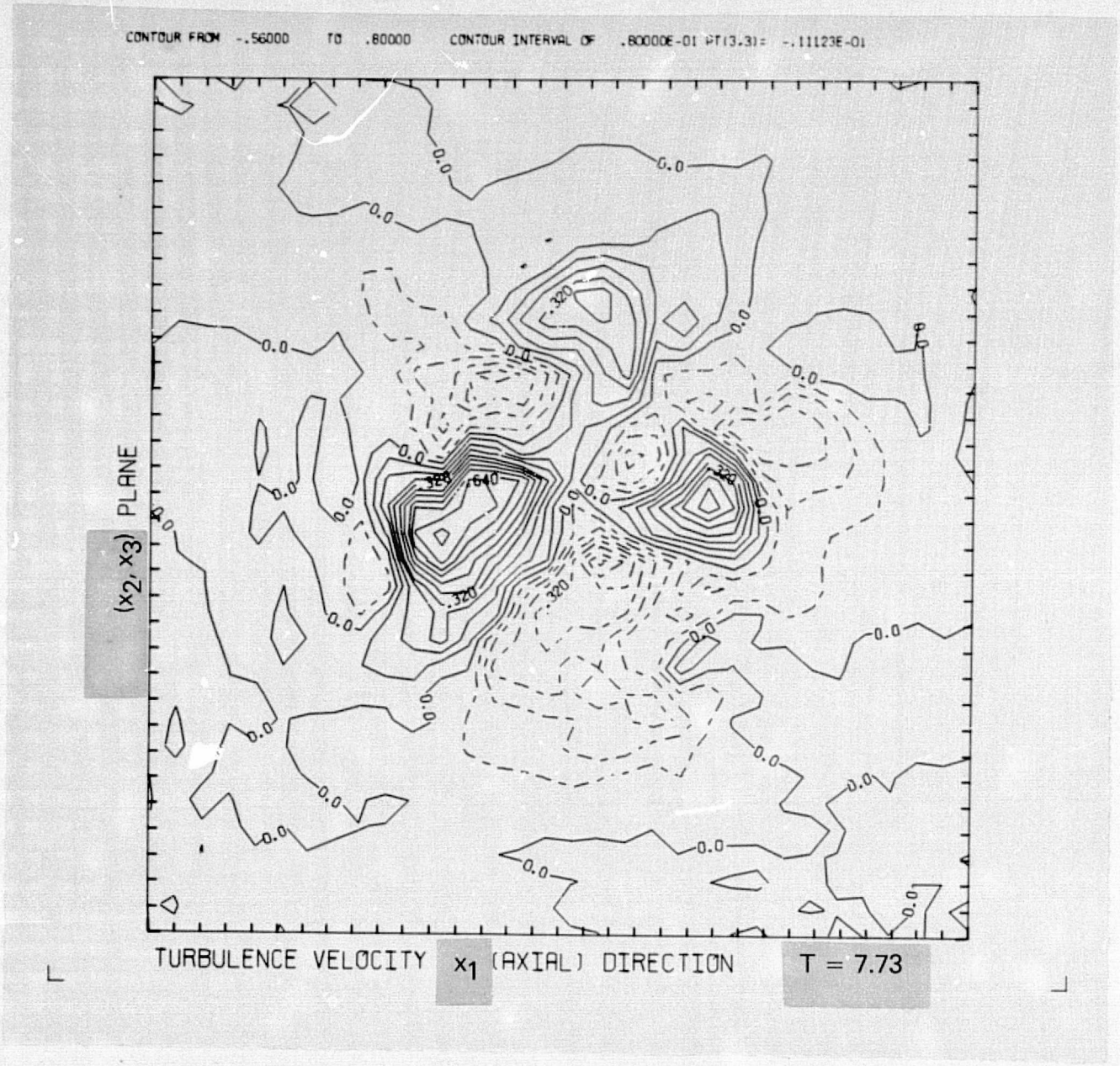

Figure 12. Velocity Field Contour Plot.

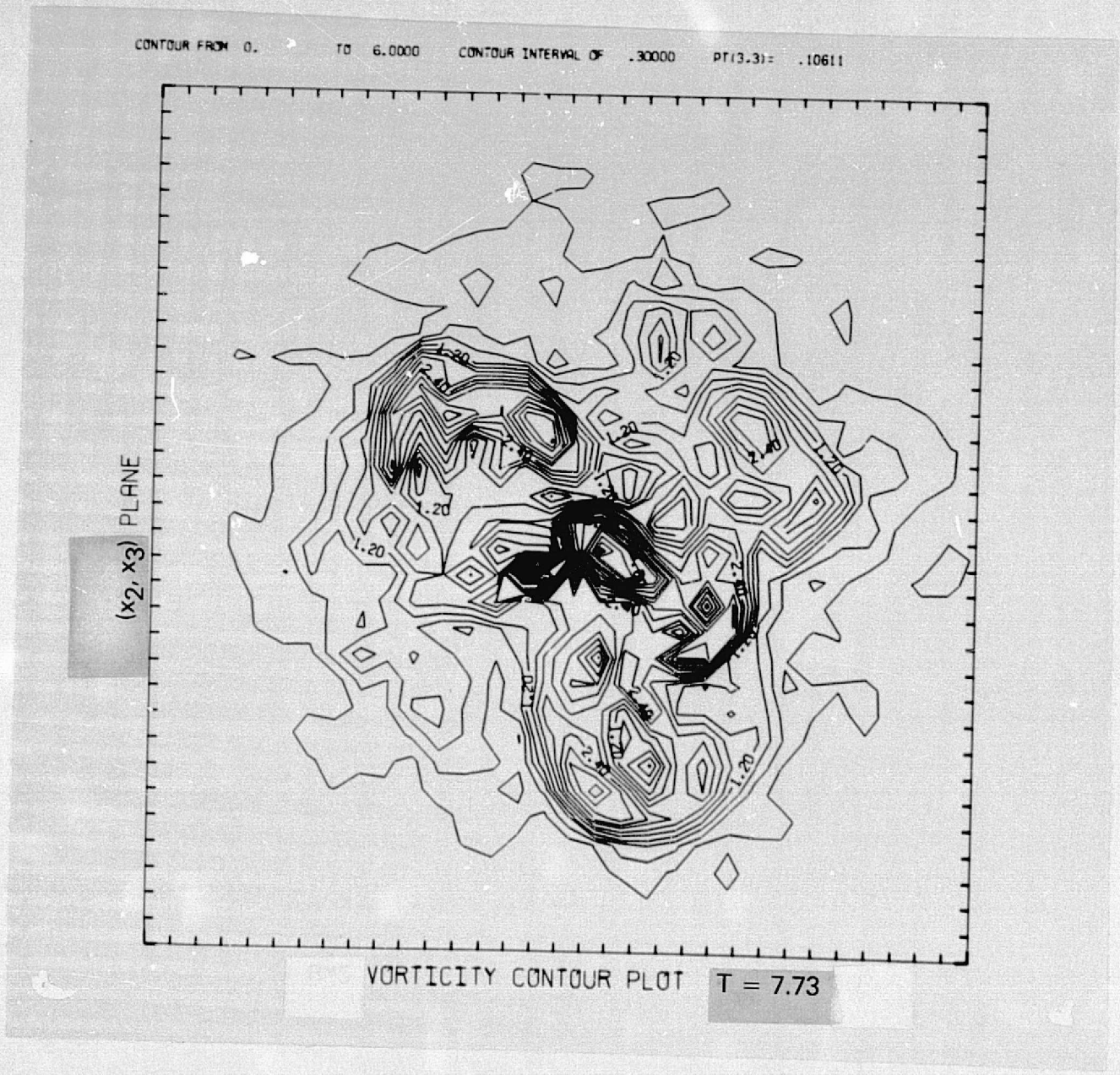

Figure 13. Vorticity Magnitude Contour Plot.

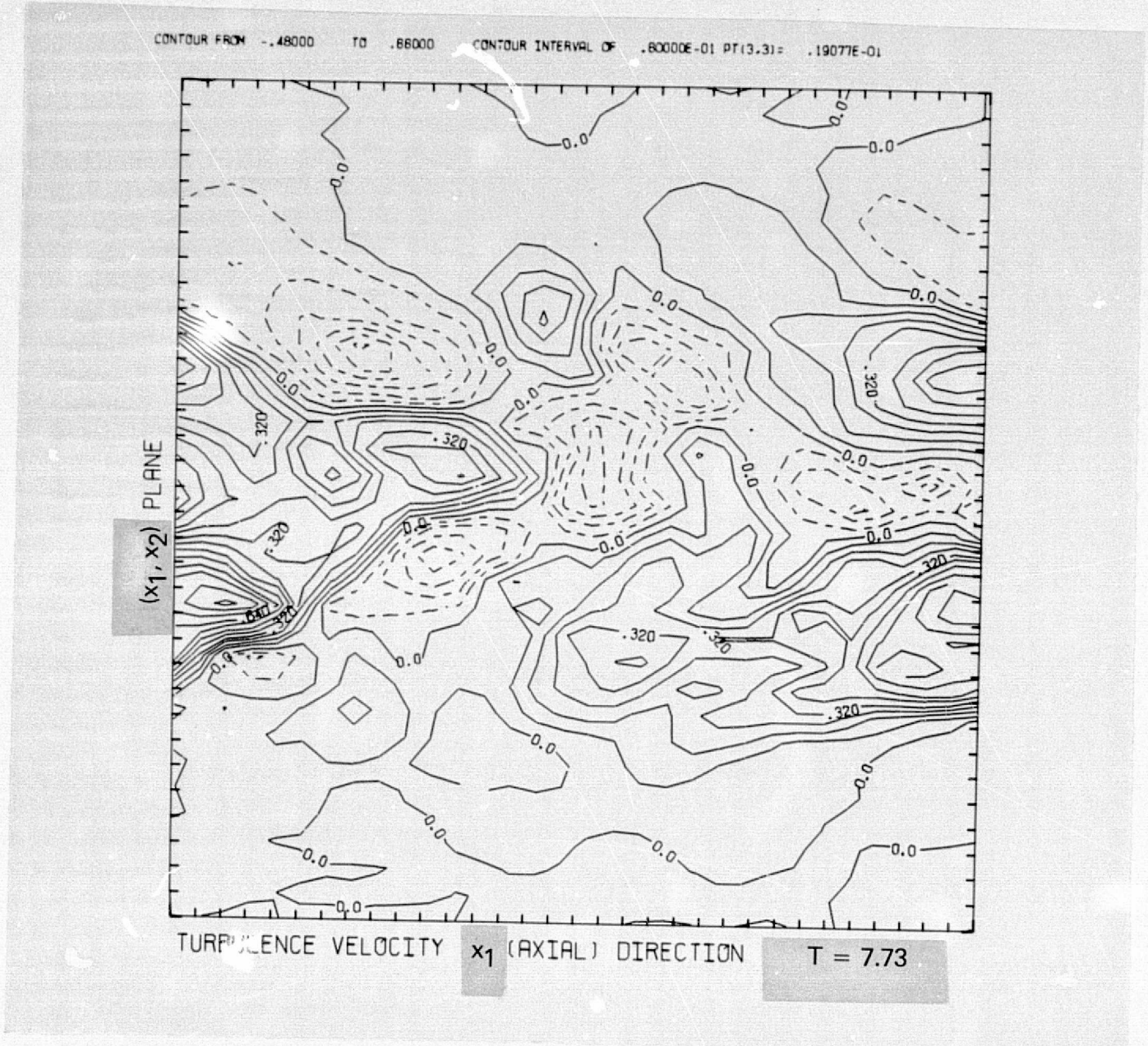

Figure 14. Velocity Field Contour Plot.

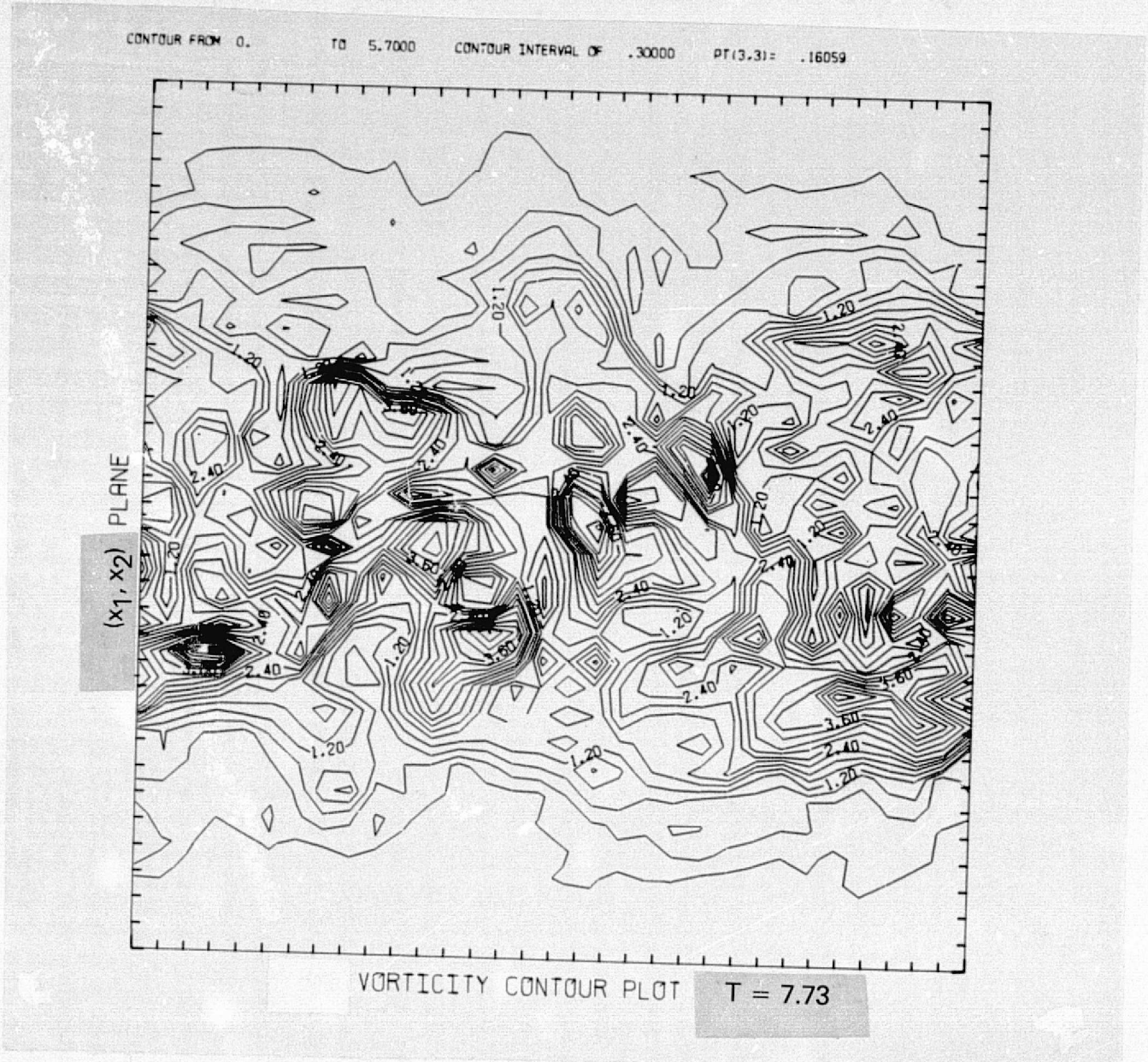

Figure 15. Vorticity Magnitude Contour Plot.

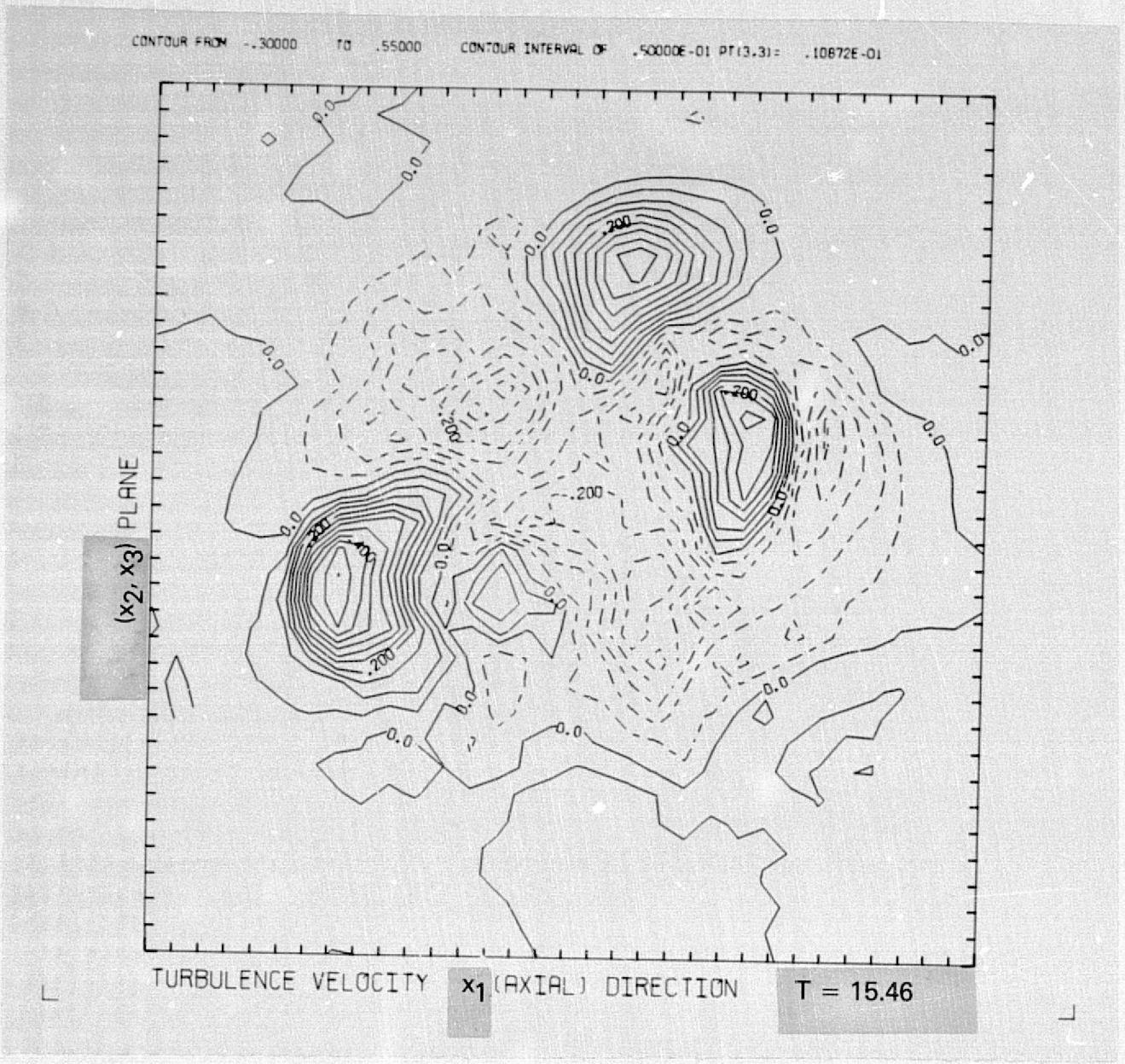

Figure 16. Velocity Field Contour Plot.

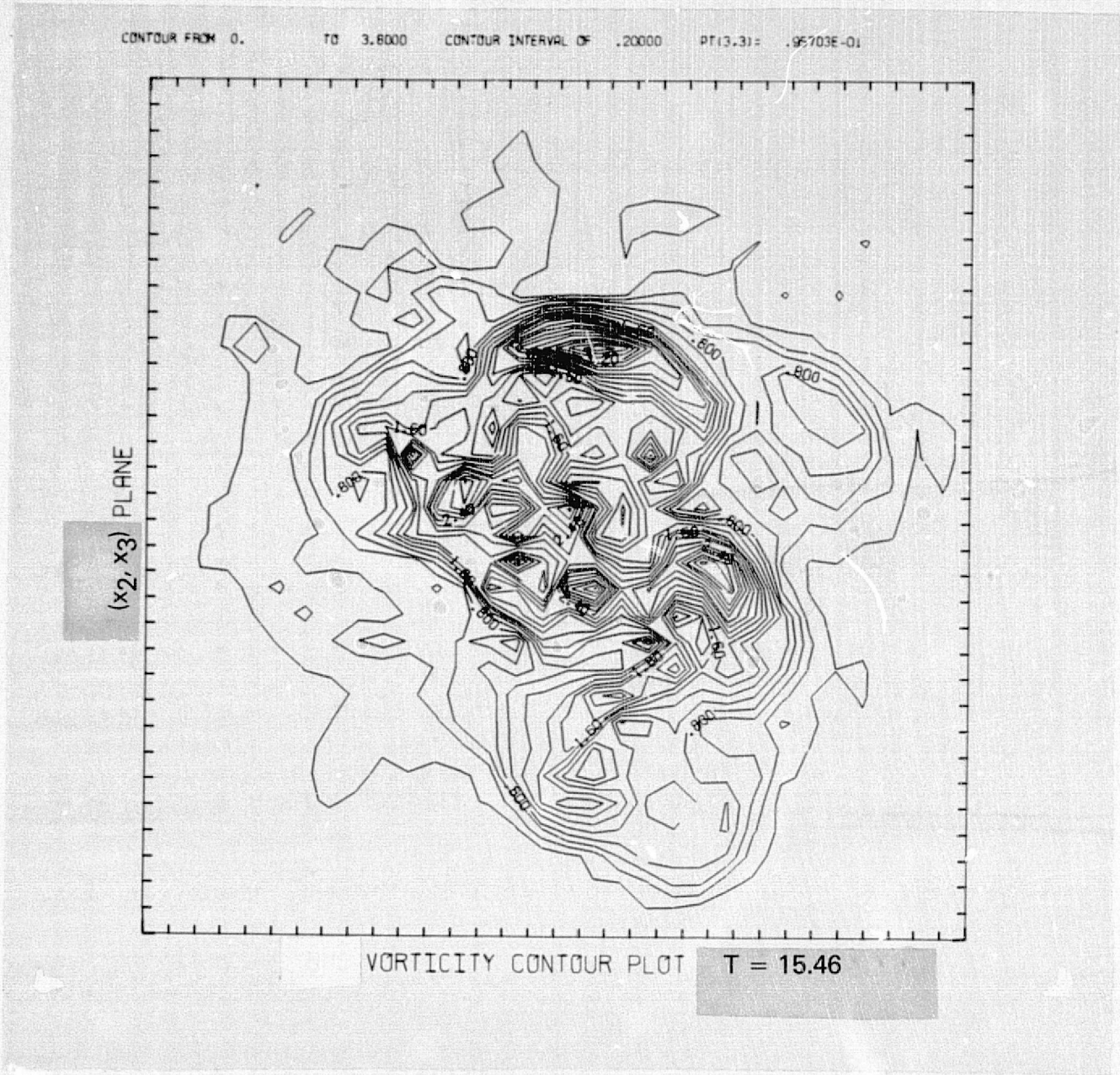

Figure 17. Vorticity Magnitude Contour Plot.

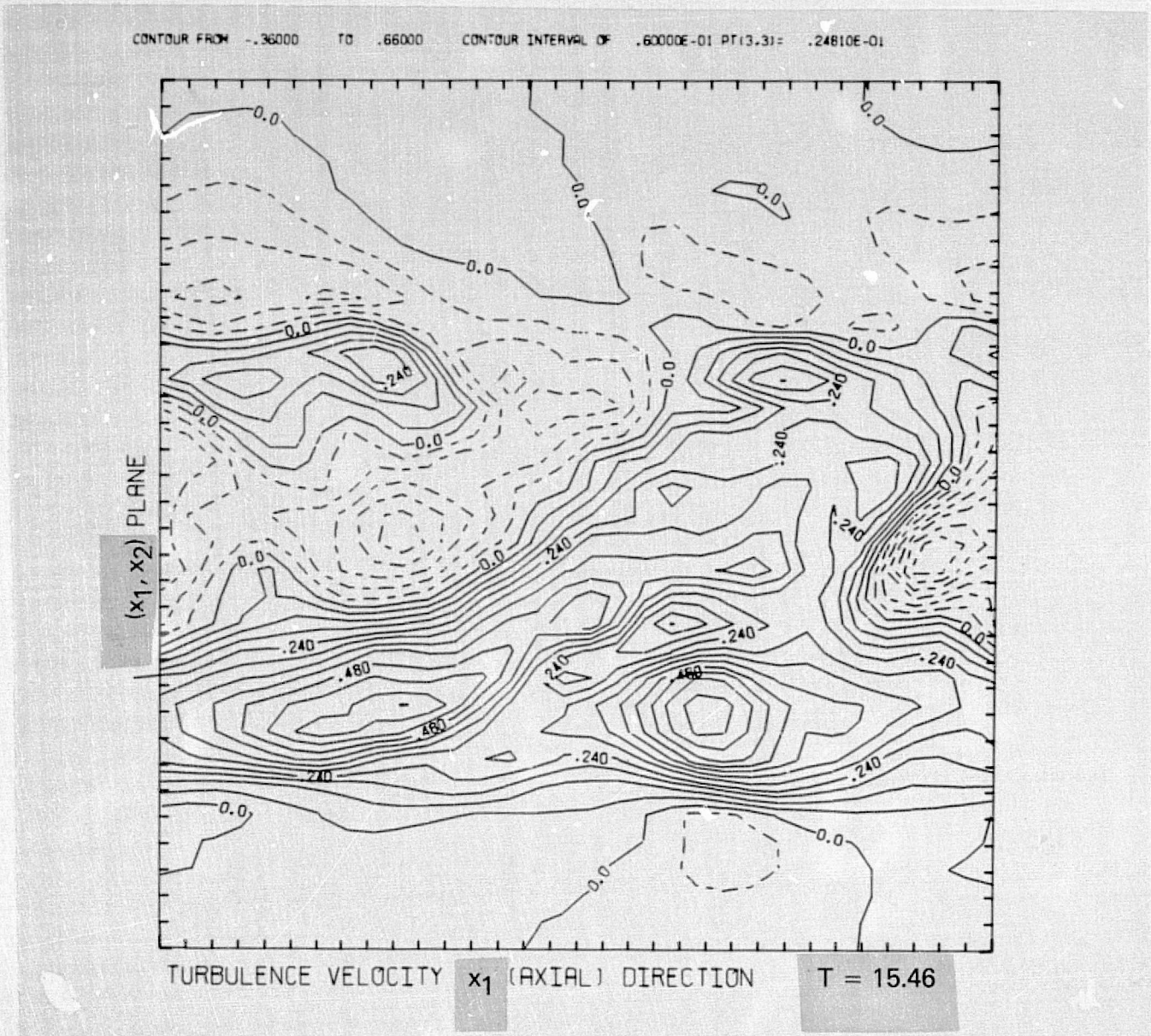

Figure 18. Velocity Field Contour Plot.

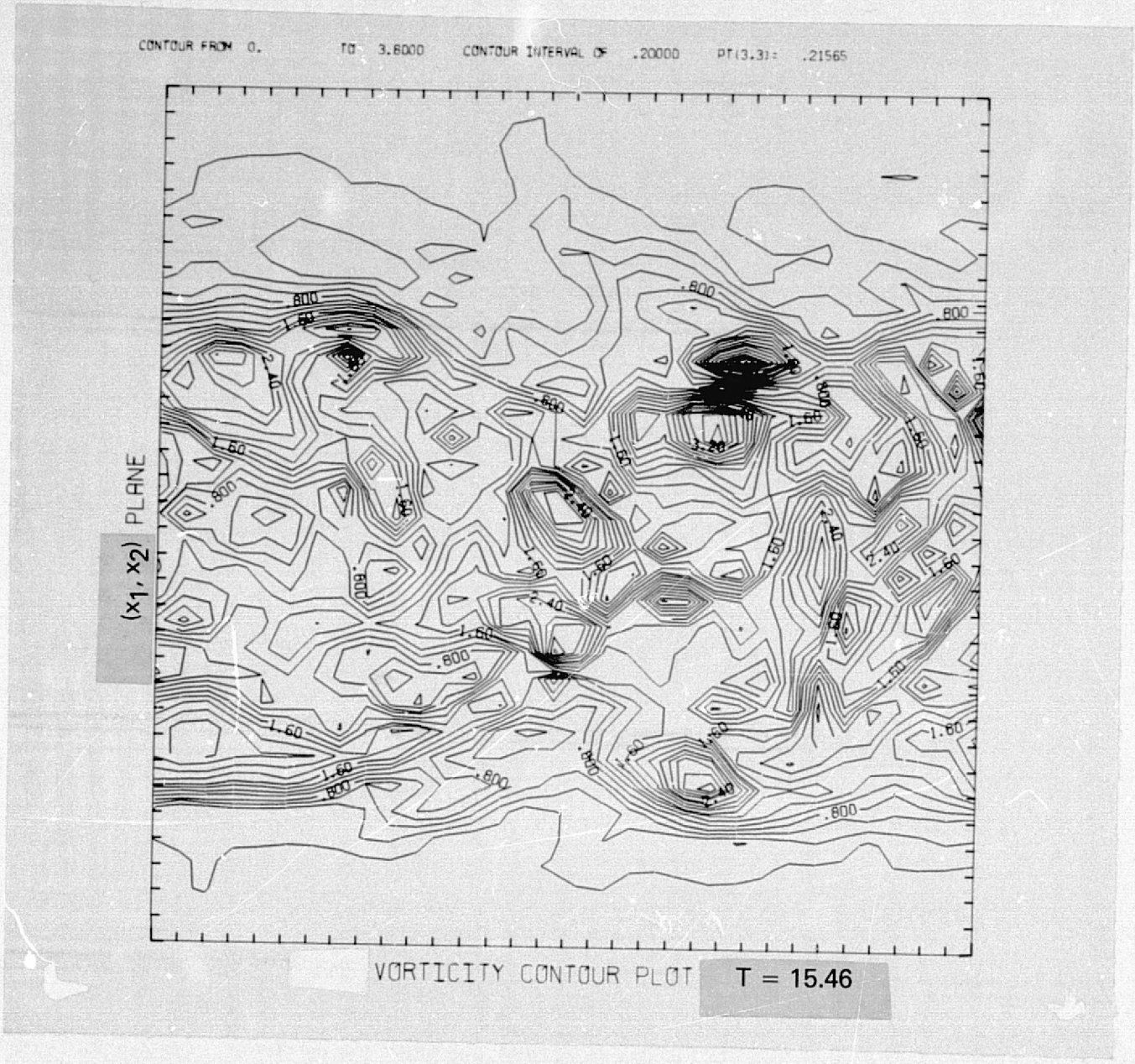

Figure 19. Vorticity Magnitude Contour Plot.

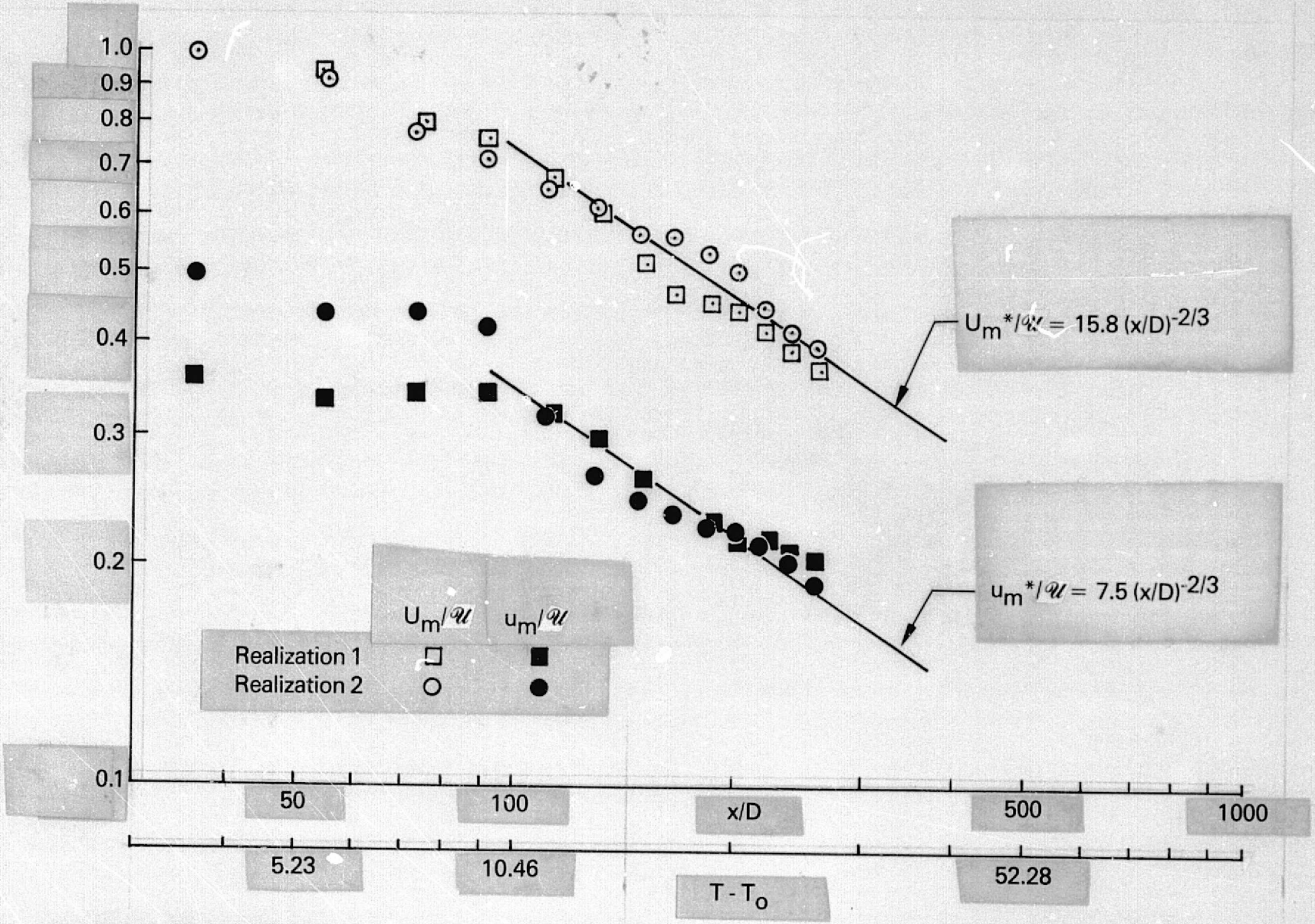

Figure 20. Decay of Maximum Mean Velocity (U_m) and Maximum Axial Turbulent Intensity (u_m).

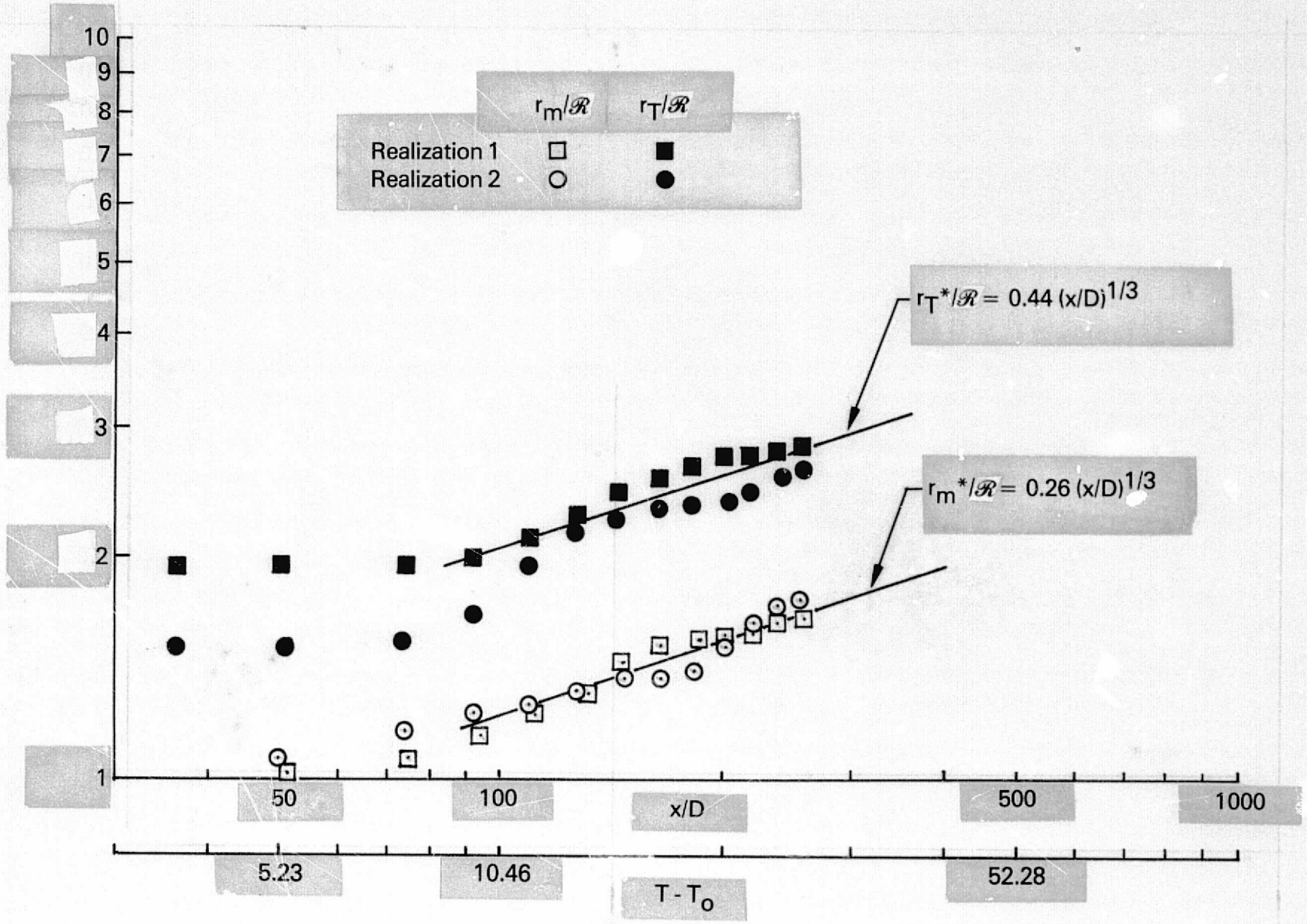

Figure 21. Growth of Mean Wake Radius (r_m) and Turbulent Wake Radius (r_T).

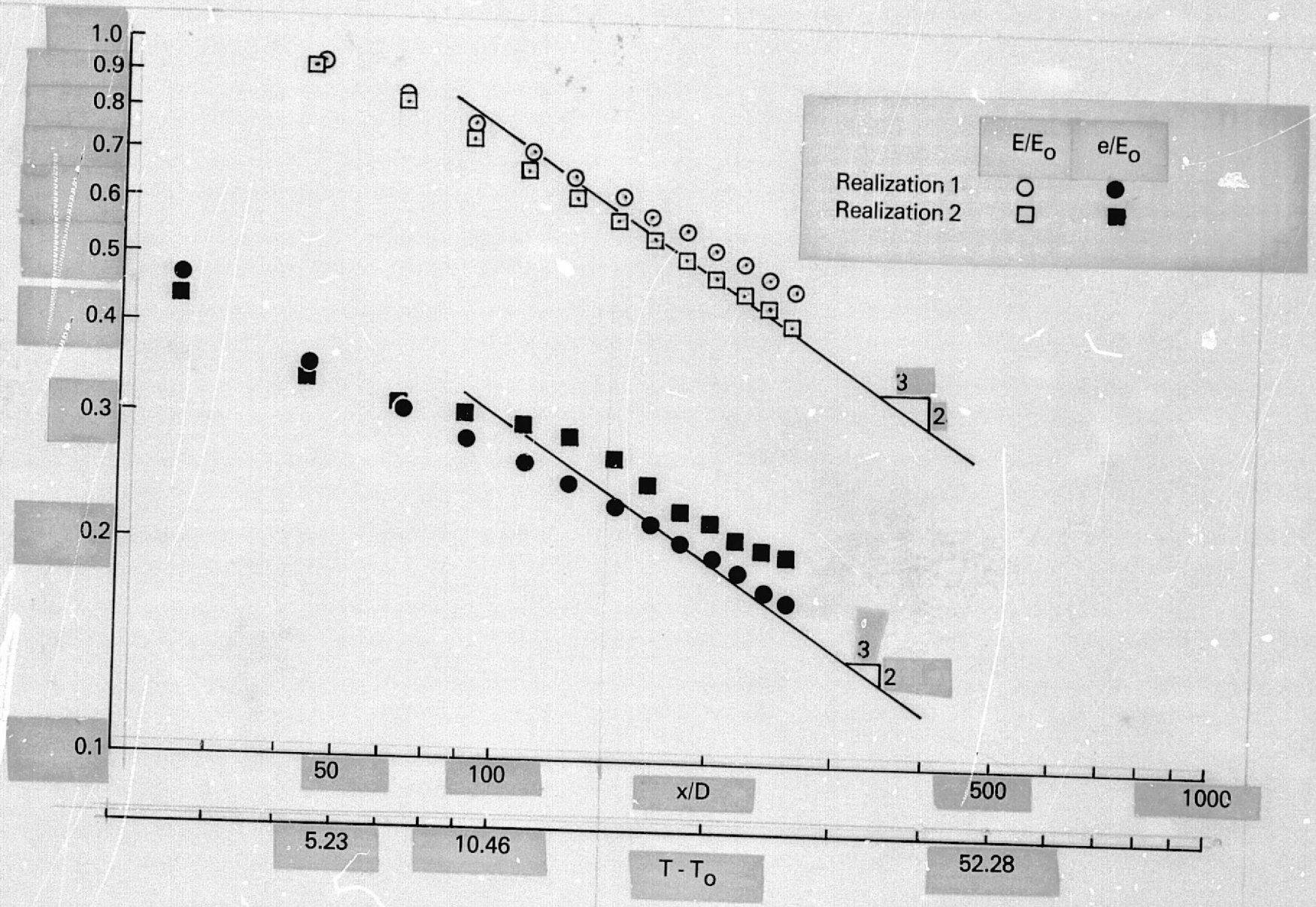

Figure 22. Decay of Integrated Mean and Turbulent Energies.

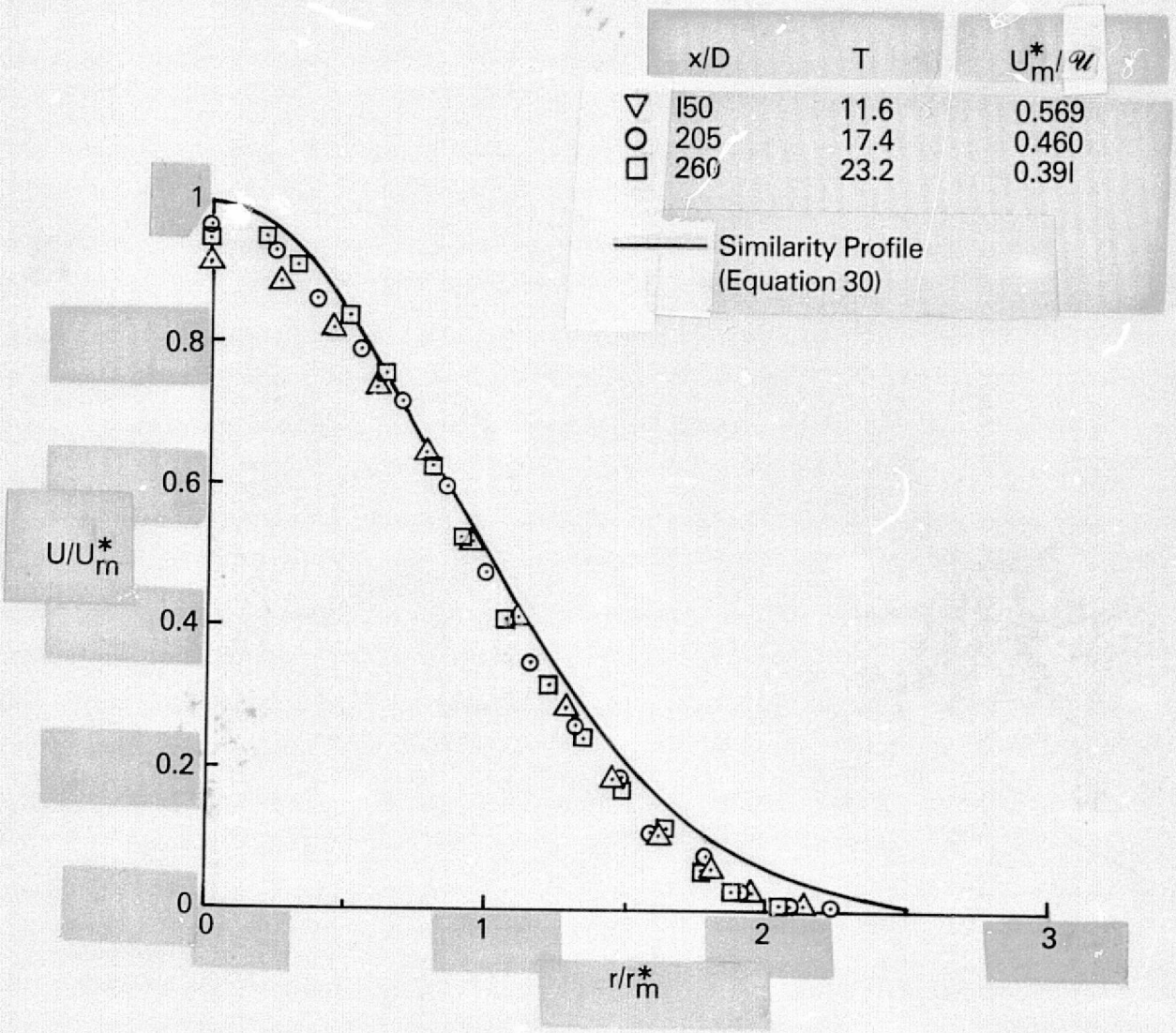

Figure 23. Normalized Profile of Axial Mean Velocity for Realization 1.

Figure 24. Normalized Profile of Axial Mean Velocity for Realization 2.

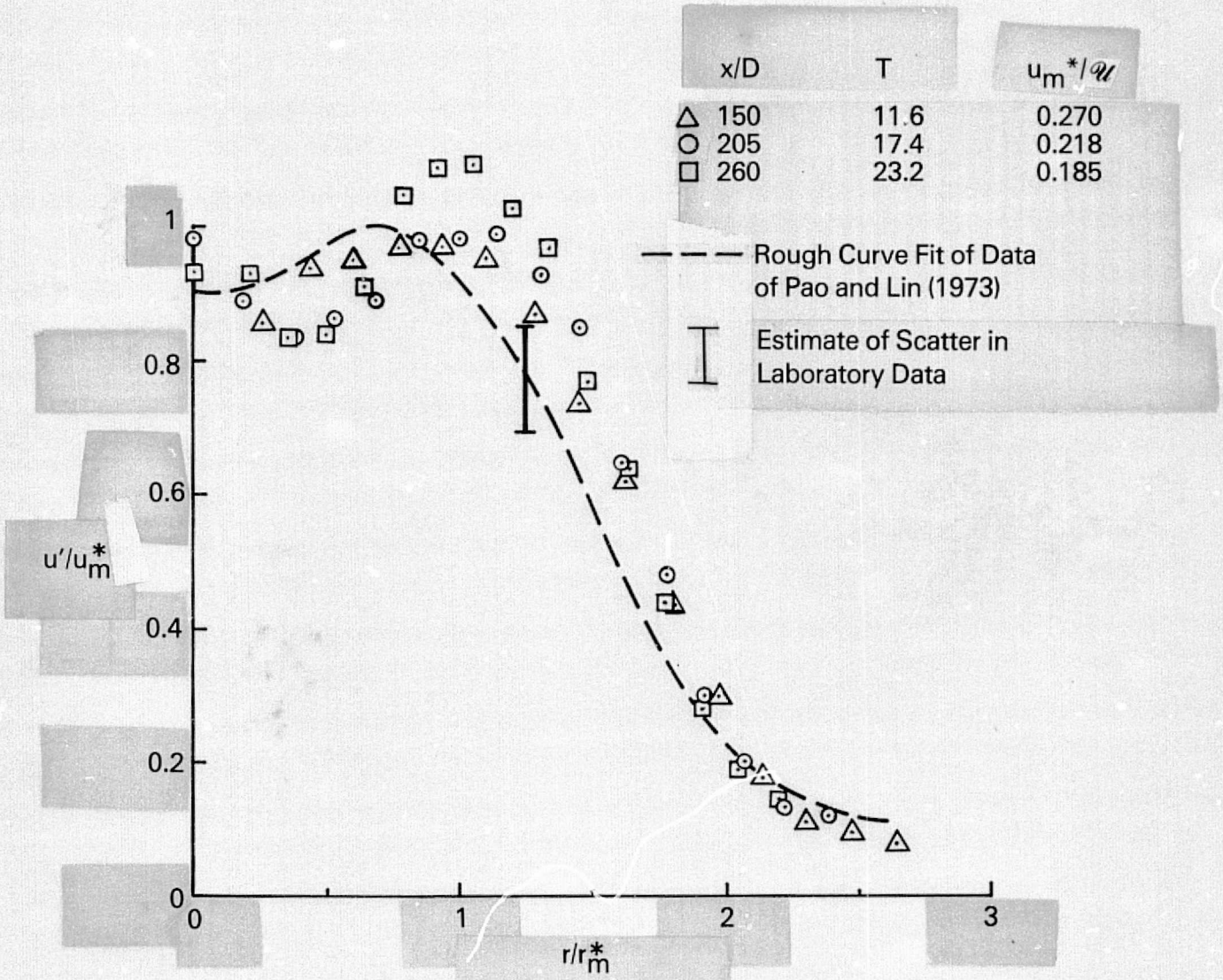

Figure 25. Normalized Profile of Axial Turbulent Intensity for Realization 1.

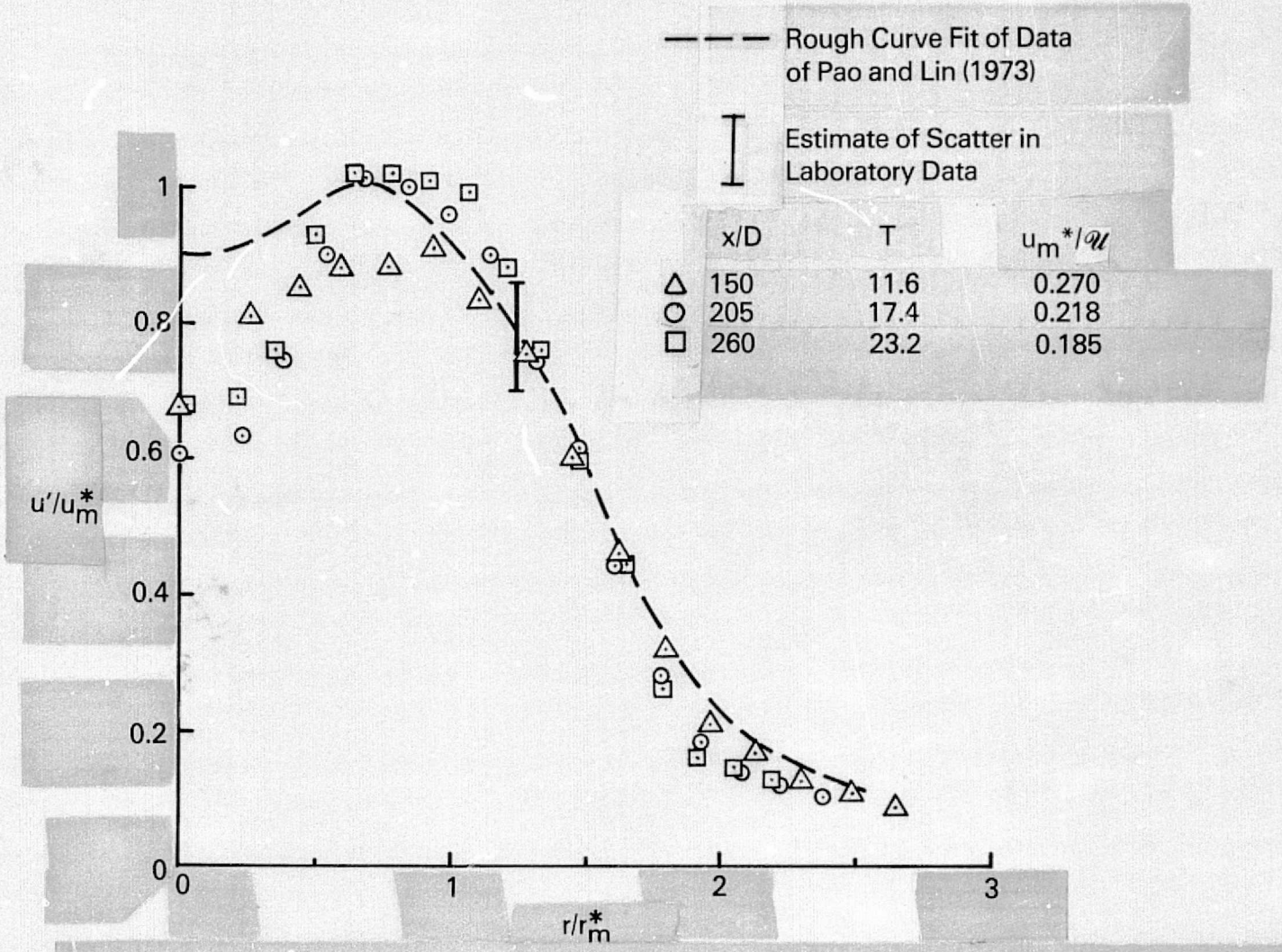

Figure 26. Normalized Profile of Axial Turbulent Intensity for Realization 2.

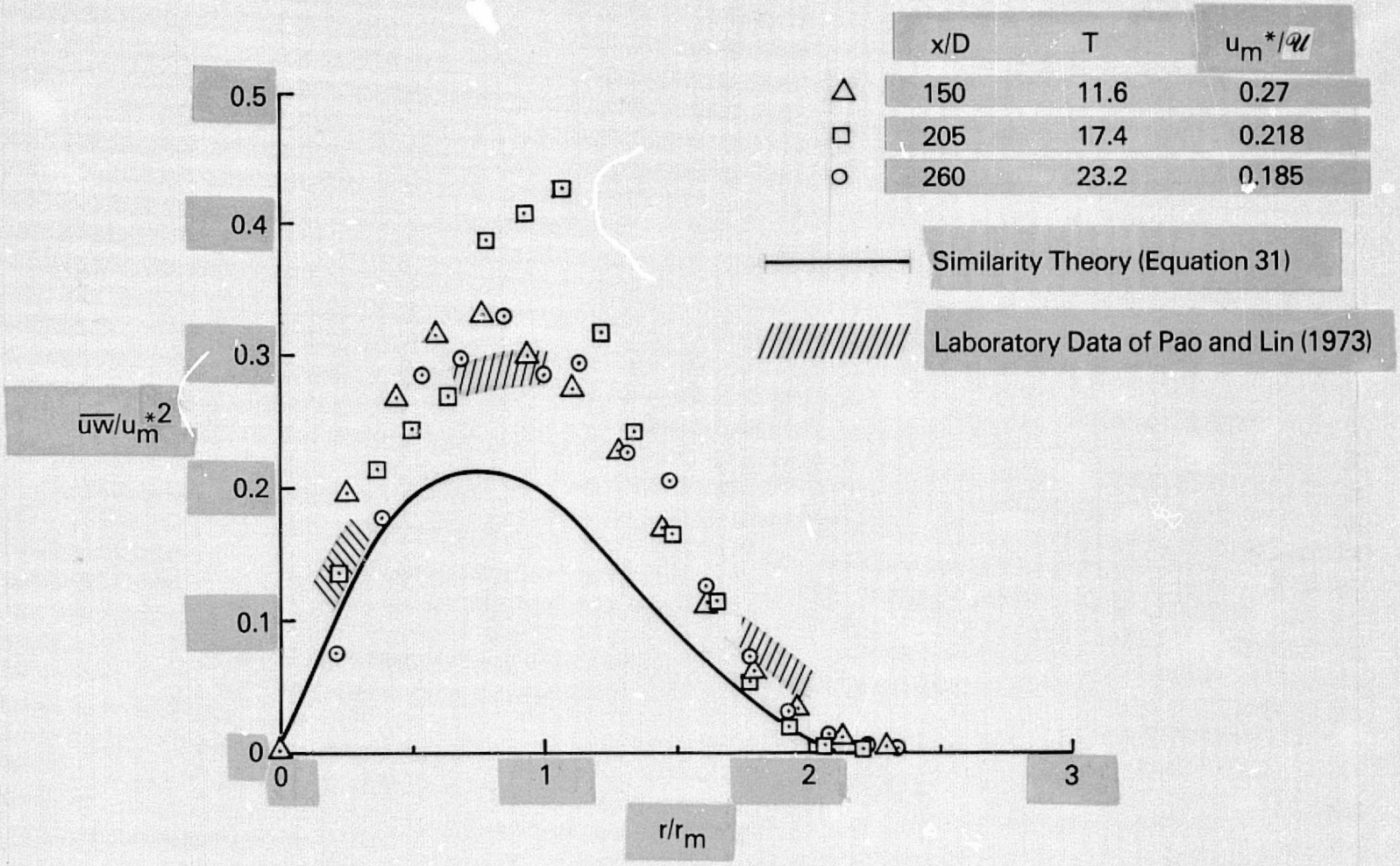

Figure 27. Normalized Profile of Reynolds Stress for Realization 1.

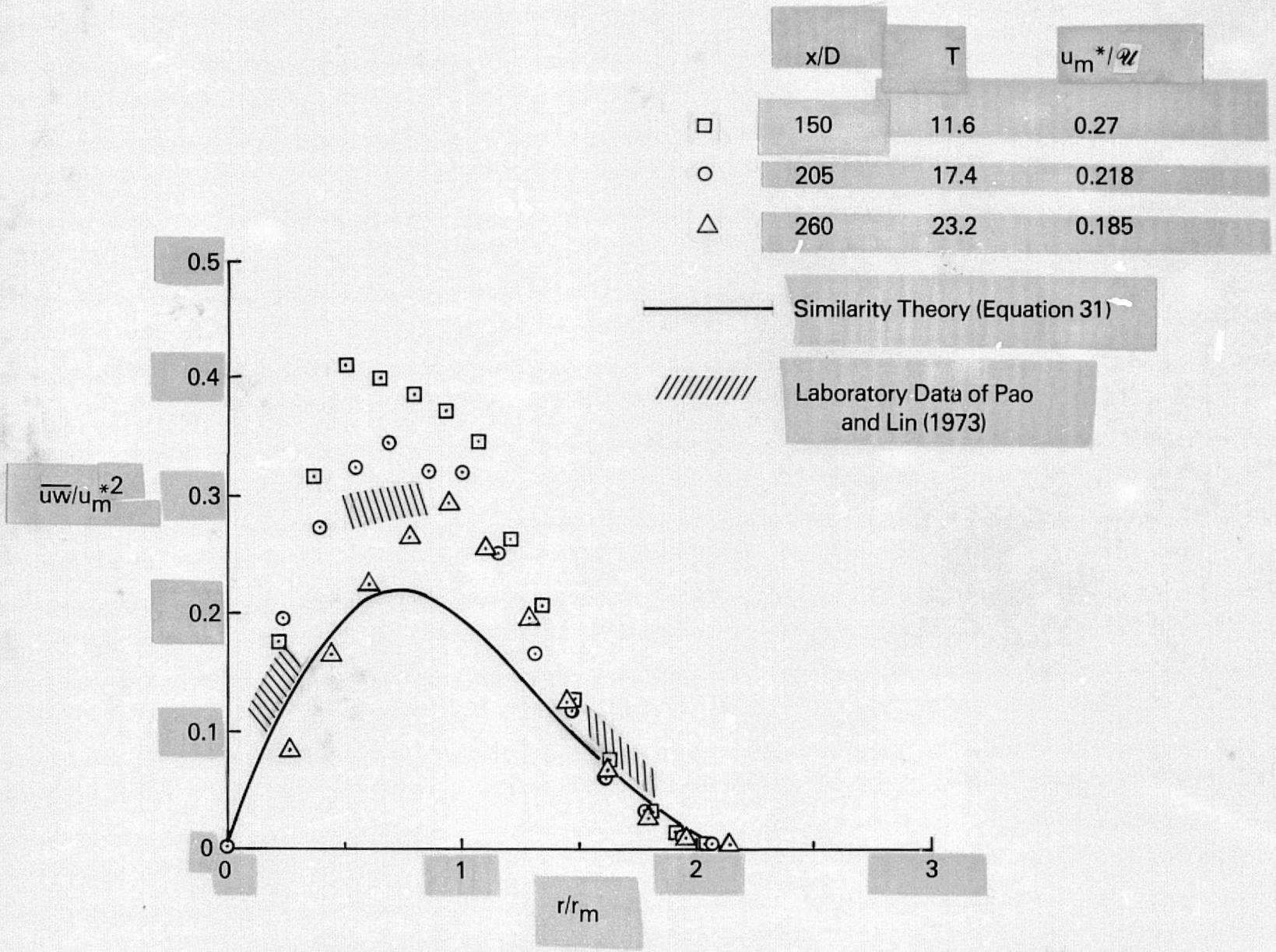

Figure 28. Normalized Profile of Reynolds Stress for Realization 2.

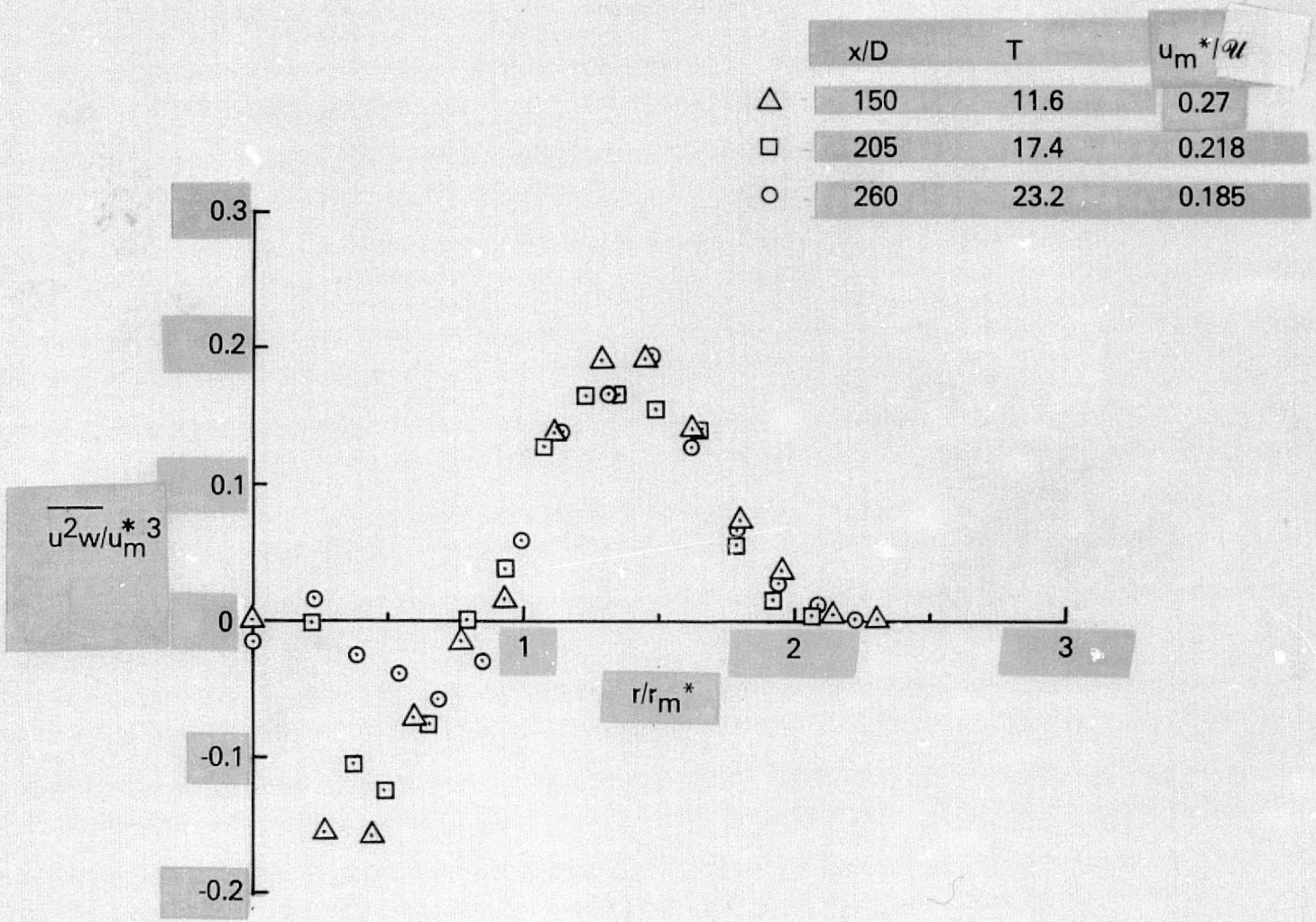

Figure 29. Normalized Profile of Radial Flux of Axial Turbulent Energy for Realization 1.

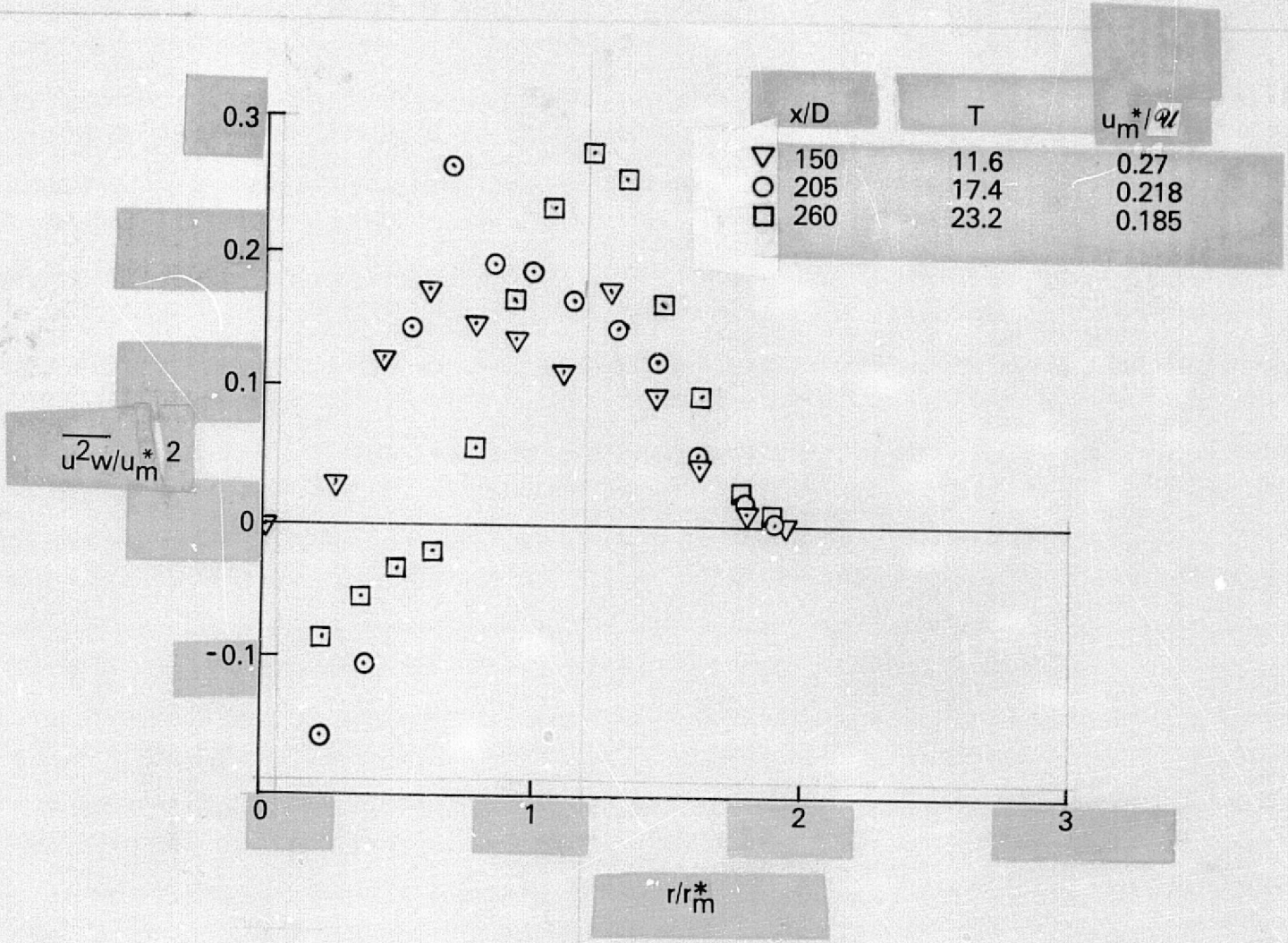

Figure 30. Normalized Profile of Radial Flux of Axial Turbulent Energy for Realization 2.

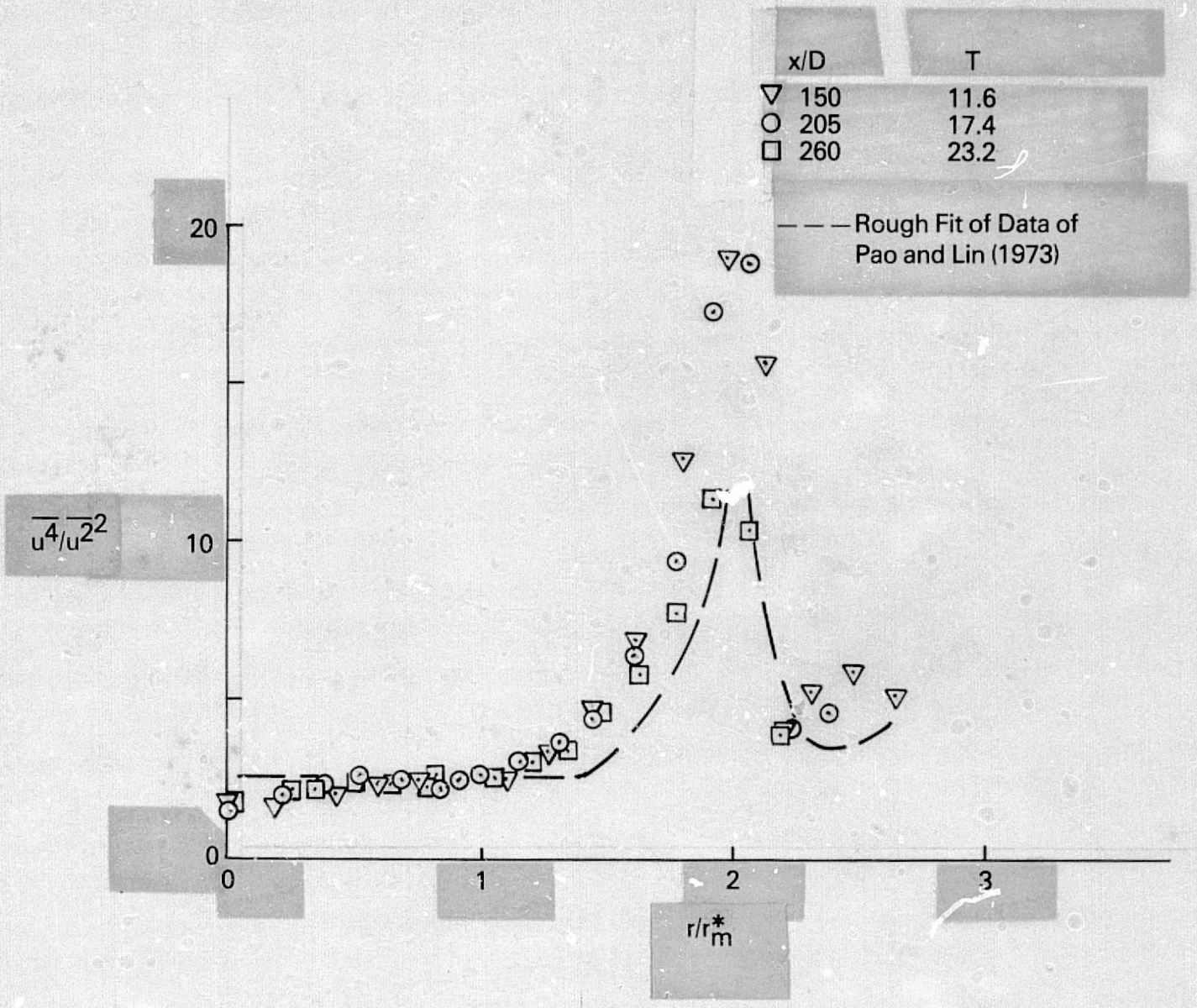

Figure 31. Profile of Velocity Kurtosis for Realization 1.

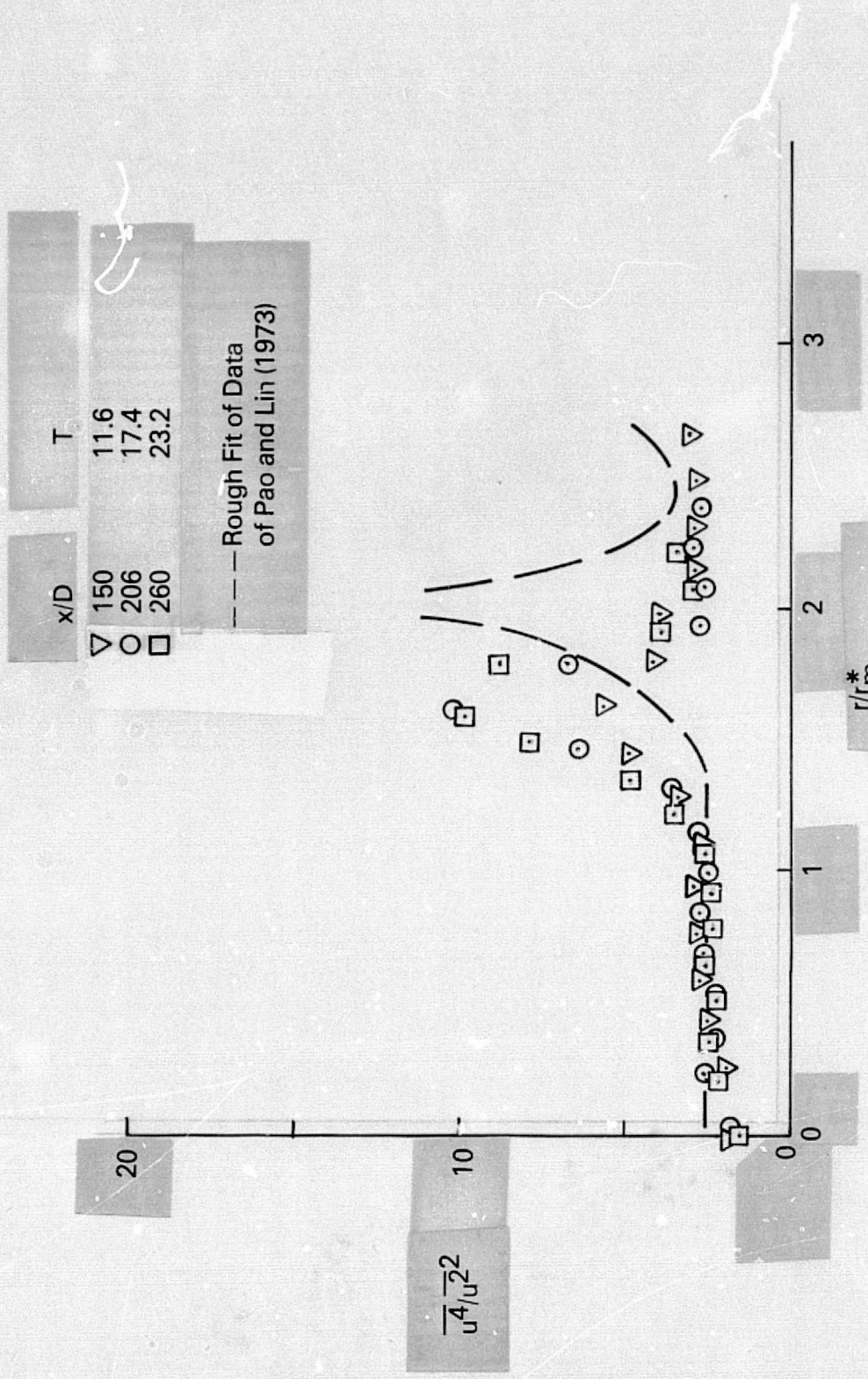

Figure 32. Profile of Velocity Kurtosis for Realization 2.

Figure 33. Profile of Velocity Skewness for Realization 1.

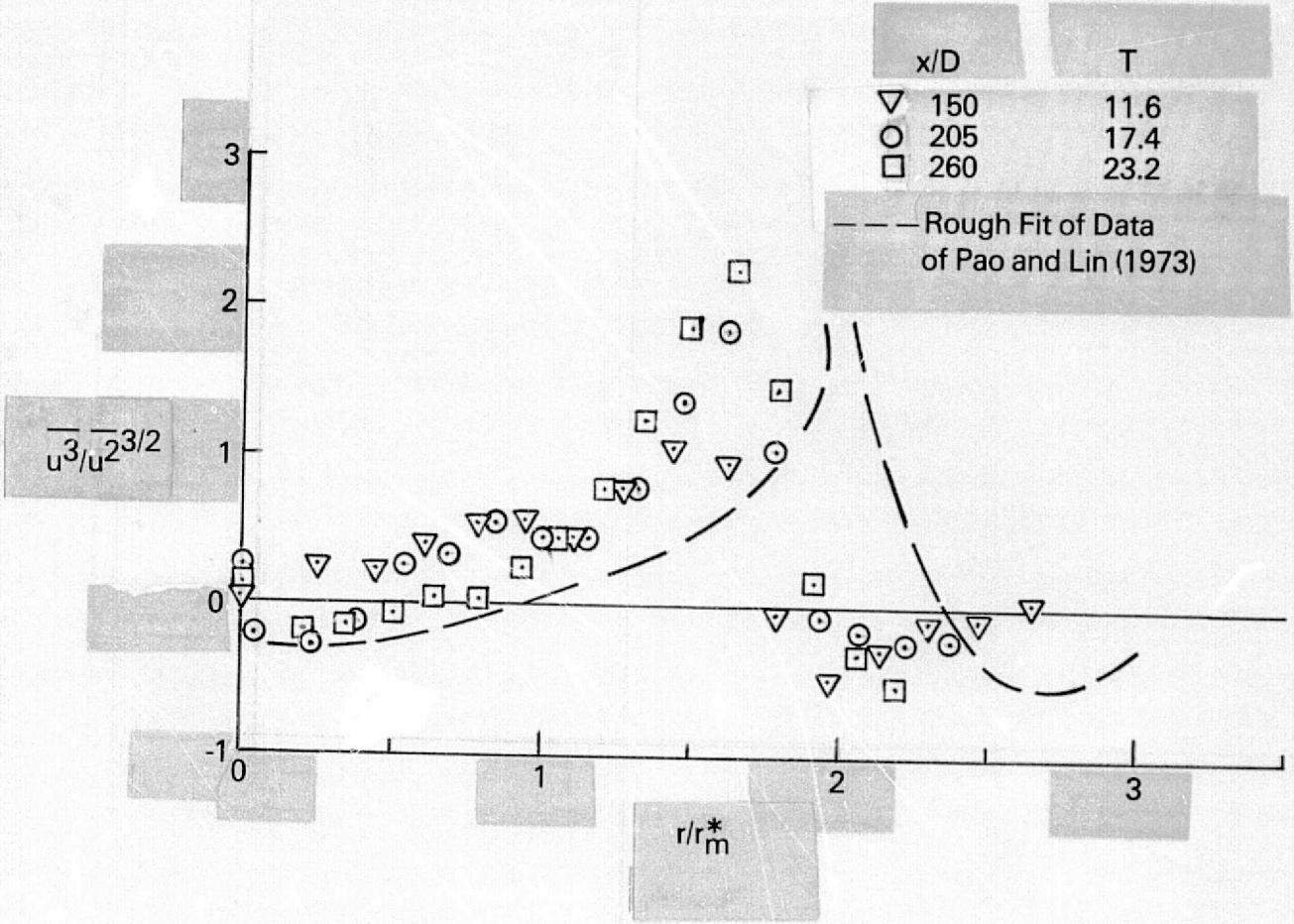

Figure 34. Profile of Velocity Skewness for Realization 2.

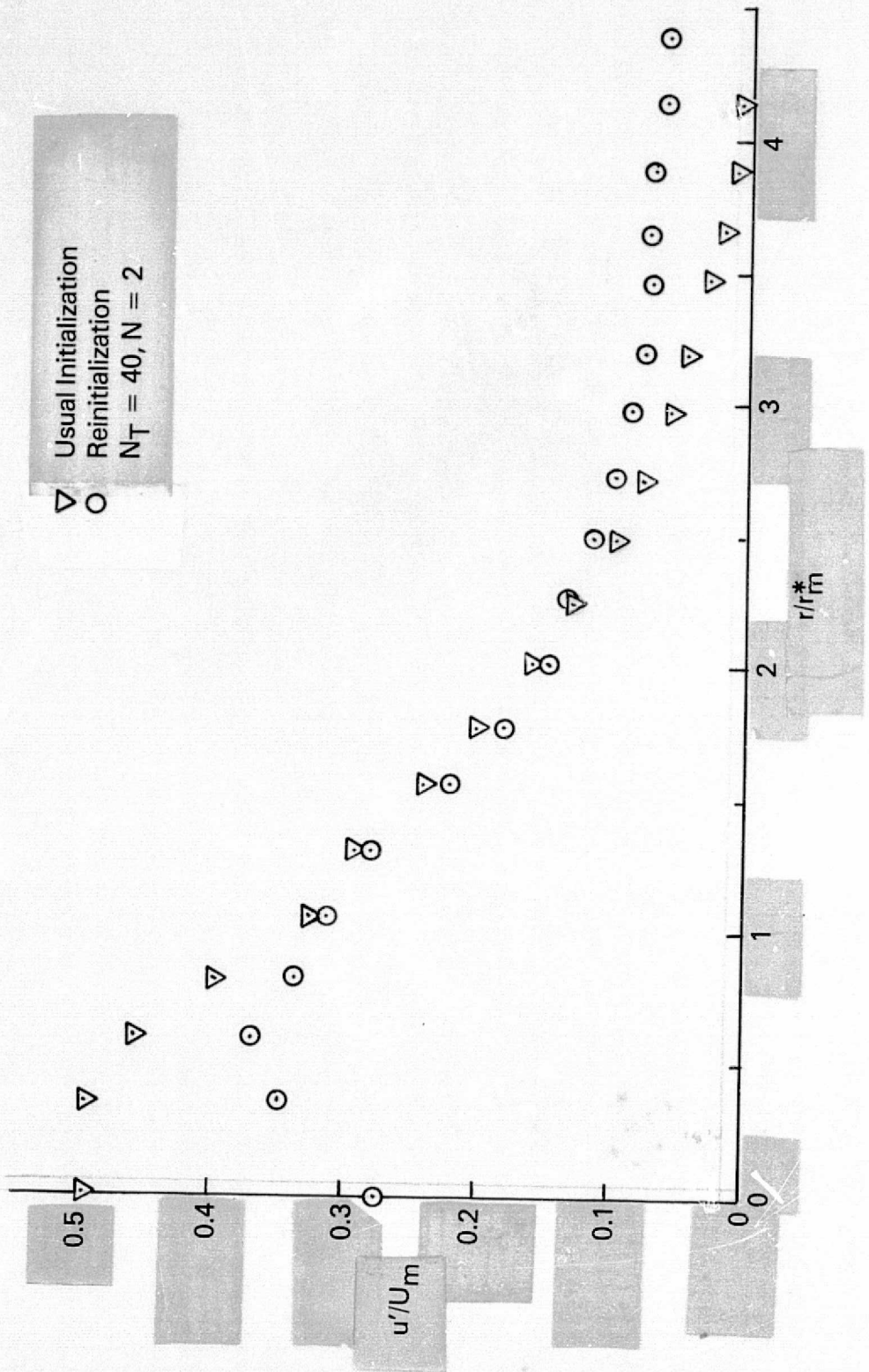

Figure 35. Initial Axial Turbulence Intensity.

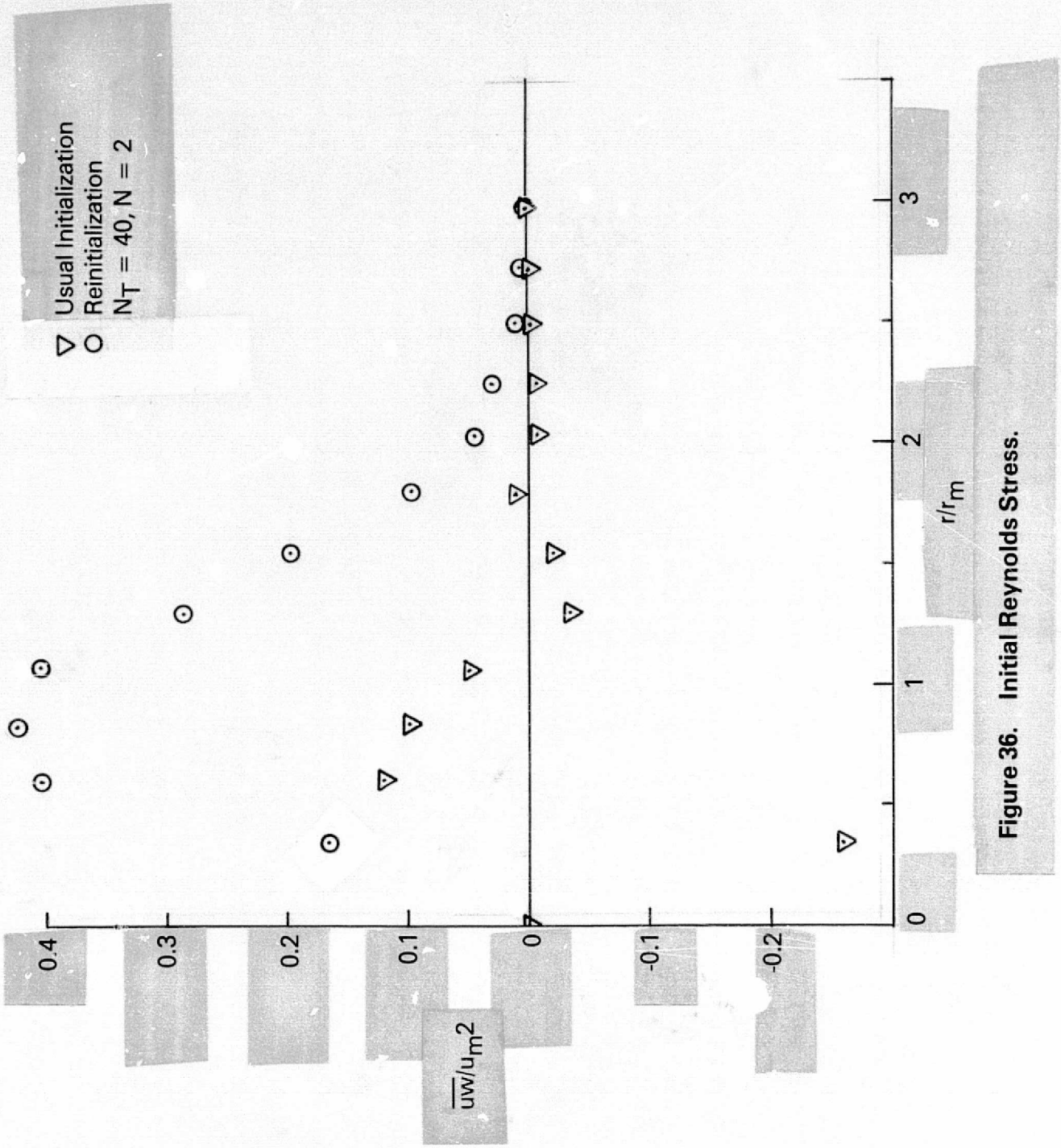

Figure 36. Initial Reynolds Stress.